

1 A dataset of vertical profiles of O₃ and HONO from the hyperspectral
2 vertical remote sensing network in China (2021-2024)

3 Tiliang Zou^{1,#}, Chengzhi Xing^{2,#,*}, Xiangguang Ji^{3,*}, Shaocong Wei⁴, Wei
4 Tan², Haoran Liu³, Cheng Liu^{2,3,5,6,7,*}

5 ¹ School of Environmental Science and Optoelectronic Technology, University of Science and
6 Technology of China, Hefei 230026, China

7 ² Key Lab of Environmental Optics & Technology, Anhui Institute of Optics and Fine Mechanics,
8 Hefei Institutes of Physical Science, Chinese Academy of Sciences, Hefei, 230031, China

9 ³ Institute of Physical Science and Information Technology, Anhui University, Hefei 230601,
10 China

11 ⁴ Institute of Environment Hefei Comprehensive National Science Center, Hefei, 230031, China

12 ⁵ Department of Precision Machinery and Precision Instrumentation, University of Science and
13 Technology of China, Hefei 230026, China

14 ⁶ Center for Excellence in Regional Atmospheric Environment, Institute of Urban Environment,
15 Chinese Academy of Sciences, Xiamen 361021, China

16 ⁷ Key Laboratory of Precision Scientific Instrumentation of Anhui Higher Education Institutes,
17 University of Science and Technology of China, Hefei 230026, China

18
19 # These authors contributed equally to this work.

20 *Corresponding to: Chengzhi Xing (xingcz@aiofm.ac.cn); Xiangguang Ji (xgji@ahu.edu.cn);
21 Cheng Liu (chliu81@ustc.edu.cn)

22

23 Abstract

24 Photolysis of HONO and O₃ in the troposphere is [a-one of the](#) primary sources of
25 OH radical and a fundamental control on atmospheric oxidative capacity. Their
26 vertical distributions and diurnal evolution are therefore essential for elucidating
27 photochemical processes in the planetary boundary layer and the lower free
28 troposphere. Yet long-term, continuous observations of the vertical profiles of HONO,
29 O₃, their photolysis frequencies, and the resulting OH production rates remain
30 extremely limited, particularly at multi-regional and interannual scales. Here we
31 present vertical profile measurements of HONO and O₃ acquired by the Chinese
32 Hyperspectral Vertical Remote Sensing Network during 2021–2024. The dataset
33 comprises 22 representative sites spanning urban, suburban, plateau, and basin
34 environments, covering diverse surface and climatic regimes. Profiles extend from the
35 surface to 4 km with ~100 m vertical resolution and ~15 min temporal resolution.
36 Using the TUV model with co-retrieved aerosol and trace-gas profiles, we derive
37 photolysis frequencies of HONO and O₃ and the corresponding OH production rates,
38 P(OH)_{HONO} and P(OH)_{O₃}. The observations reveal robust regional patterns in the
39 diurnal and vertical structure of tropospheric photochemical activity. Photolysis
40 frequencies peak near local noon and generally increase with altitude from the surface
41 layer to the upper mixed layer and the lower free troposphere, whereas OH production
42 rates reach their maxima within the boundary layer and decrease with height.
43 Processed using a unified retrieval framework and rigorous quality control, this
44 dataset provides quantitative constraints on the contribution of HONO and O₃
45 photolysis to tropospheric OH, supports improved radical parameterizations in
46 chemical transport models, and enables synergistic multi-platform remote sensing
47 analyses. By delivering the first systematic, long-term vertical profiles of HONO, O₃,
48 and their OH production in China, this public dataset fills a critical observational gap
49 and offers a robust basis for investigating the spatiotemporal evolution of tropospheric
50 oxidative capacity across regions and altitude ranges, with substantial scientific
51 significance and long-term applicability. The dataset is available for free at Zenodo
52 (<https://doi.org/10.5281/zenodo.18489836>, Zou et al., 2026)

54 1. Introduction

55 Over the past decade, “the implementation of China’s Air Pollution Prevention
56 and Control Action Plan” (2013) and “the Three-Year Action Plan for Defending the
57 Blue Sky” (2018) has led to a marked reduction in fine particulate matter (PM_{2.5})
58 nationwide (Liu et al., 2023b; Wang et al., 2020). In contrast, ozone (O₃)—a
59 secondary pollutant and a major atmospheric oxidant—has continued to increase [on](#)
60 [average, particularly](#) in economically developed regions such as the Beijing–Tianjin–
61 Hebei area, the Yangtze River Delta, and the Pearl River Delta, where it has emerged
62 as the most intractable air-quality problem after PM_{2.5} (Guo et al., 2023; He et al.,
63 2023a; Li et al., 2020; Lyu et al., 2025; Zou et al., 2025). [To address the observational](#)
64 [gaps in these and other key regions, we developed a comprehensive dataset. The](#)

65 [dataset comprises measurements from 22 ground-based sites across five major regions](#)
66 [of China—North, East, Southwest, South, and Central China.](#) Photochemical air
67 pollution is a dominant driver of urban and regional air-quality degradation,
68 characterized by the rapid sunlight-driven accumulation of secondary species, most
69 notably O₃ (Dewan and Lakhani, 2022; Donzelli and Suarez-Varela, 2024; Sharma et
70 al., 2025; Wang et al., 2025b). Beyond being a typical secondary pollutant, O₃ is a
71 powerful oxidant that exerts substantial impacts on regional climate, ecosystems, and
72 human health (Monks et al., 2015; Sharma et al., 2025; Wang et al., 2025b; Xing et al.,
73 2017). Nitrous acid (HONO), a short-lived reactive nitrogen species, occurs at
74 relatively low concentrations but represents a major primary source of the OH radical,
75 the key “detergent” of the troposphere (Andersen et al., 2023; He et al., 2023c; Song
76 et al., 2023a; Zhang et al., 2023a). In polluted environments, photolysis of HONO can
77 account for 20–80% of total OH production, and its relative importance is particularly
78 pronounced during early morning and late afternoon, when solar elevation is low and
79 alternative OH sources are less efficient (Elshorbany et al., 2010; He et al., 2023c;
80 Zhang et al., 2023a). A quantitative understanding of the formation and transport of
81 both HONO and O₃ is therefore essential for elucidating the mechanisms of
82 tropospheric photochemical pollution and for designing effective mitigation strategies.

83 Despite extensive research on HONO and O₃, major gaps persist in observations
84 of their vertical structure and in the parameterization of key photochemical processes,
85 limiting a mechanistic understanding of photochemical air pollution (Liu et al., 2023a;
86 Wang et al., 2018, 2025c; Zhang et al., 2024; Zhu et al., 2025b). Vertical
87 measurements remain particularly sparse, and concurrent profiles of HONO and O₃
88 are largely unavailable (Garcia-Nieto et al., 2018a; Song et al., 2023a; Wang et al.,
89 2018, 2025c; Zhu et al., 2025b). China National Environmental Monitoring Center
90 (CNEMC), with more than 2,000 surface stations, provides routine measurements of
91 PM_{2.5}, NO₂, and SO₂, but ~~generally~~ lacks observations of key photochemical
92 precursors such as HONO and volatile organic compounds (VOCs) (Liu et al., 2023a;
93 Qu et al., 2020; Zhang et al., 2024; Zhu et al., 2025b). More fundamentally, surface
94 observations alone cannot resolve pollutant distributions within the planetary
95 boundary layer or capture variations in vertical atmospheric structure (Wang et al.,
96 2018, 2019, 2025c; Xuan et al., 2025a; Zhu et al., 2025b), and exclusive reliance on
97 near-surface data may therefore bias assessments of regional transport and
98 accumulation (Liu et al., 2023a; Wang et al., 2019, 2025c). Spaceborne sensors,
99 including MODIS, CALIPSO, TROPOMI, and OMI, provide global fields of aerosol
100 optical depth (AOD) and vertical column densities (VCDs) for selected trace gases.
101 However, their limited temporal sampling and spatial resolution preclude resolving
102 the ~~fine-scale pronounced~~ diurnal variability and fine vertical structure of O₃ and
103 HONO (Itahashi et al., 2020; Johnson et al., 2024; Torres et al., 2020a; Wang et al.,
104 2025a). Chemical transport models (CTMs) and regional climate models (RCMs) can
105 reproduce the spatiotemporal evolution of pollutants, but their performance depends
106 critically on initial and boundary conditions, and uncertainties in vertical

设置了格式: 下标

107 parameterizations—such as turbulent mixing and chemical mechanisms—often lead
108 to substantial biases in simulated profiles (Chambers et al., 2019; Kim et al., 2024; Li
109 et al., 2021; Sekiya et al., 2025; Thürkow et al., 2024). Current in situ and remote-
110 sensing techniques also have intrinsic limitations. Lidar systems provide high-
111 resolution aerosol profiles but are restricted in detectable gaseous species and spatial
112 coverage (Anon, 2023; Johnson et al., 2024; Torres et al., 2020b). Aircraft and balloon
113 soundings yield detailed upper-air observations but are expensive and unsuitable for
114 sustained, long-term monitoring (Johnson et al., 2024; Sekiya et al., 2025; Wang et al.,
115 2025a; Yu et al., 2025). Tower measurements, while valuable near the surface, are
116 height-limited and cannot capture the full vertical variability across the boundary
117 layer (Chambers et al., 2019; Kim et al., 2024; Thürkow et al., 2024).

118 To address the observational limitations and scientific questions outlined above,
119 we developed a comprehensive dataset of vertical profiles of HONO, O₃, and their
120 photolysis frequencies using the Chinese Hyperspectral Vertical Remote Sensing
121 Network. The primary objective is to resolve the vertical structure of HONO and O₃
122 and to quantify the ~~altitude-resolved~~~~altitude-dependent~~ production of OH radicals
123 from their photolysis. This dataset fills a critical gap in vertical observations of key
124 photochemical species over China and provides a unique basis for assessing the
125 contribution of HONO photolysis to boundary-layer OH ~~budget~~, the vertical
126 characteristics of O₃ formation, and the role of aerosols in modulating photolysis rates.
127 The dataset comprises measurements from 22 ground-based sites across five major
128 regions of China—North, East, ~~Southwest~~, South, ~~Central~~, and ~~Central Southwest~~
129 China—collected during 2021–2024. Its core products are high-temporal-resolution
130 vertical profiles of HONO and O₃ spanning 0–4 km. Public release of this dataset will
131 enable systematic investigations of the unresolved sources of HONO in the boundary
132 layer and the vertical variability in O₃ production sensitivity. When combined with
133 numerical models, the high-resolution vertical information can be used to evaluate
134 and refine photochemical mechanisms, quantify the contribution of HONO photolysis
135 to the tropospheric OH budget, and reduce uncertainties in vertical parameterizations.
136 These advances will, in turn, support robust source attribution of O₃ pollution and
137 inform the development of coordinated regional control strategies for PM_{2.5} and O₃.
138 The following sections describe the site distribution, observational and retrieval
139 methods, and the seasonal and diurnal features of the HONO and O₃ vertical
140 structures revealed by this dataset.

141

142 **2. Method**

143 **2.1 Description of the monitoring site**

144 The dataset is derived from 22 hyperspectral ground-based vertical remote
145 sensing stations distributed across five major regions of China—North, East,
146 ~~Southwest~~, South, ~~Central~~, and ~~Central Southwest~~—China—forming an integrated
147 network that samples a wide range of representative atmospheric environments (Table
148 1). The sites span urban cores, urban–suburban transition zones, regional background

149 areas, coastal and land–sea interaction regions, as well as plateau, mountain, and basin
150 settings, thereby providing a three-dimensional observational framework for key
151 photochemical species. In North China, stations at the Chinese Academy of
152 Meteorological Sciences (CAMS1, CAMS2) and the University of Chinese Academy
153 of Sciences (UCAS), located ~~in and around~~ within Beijing (~100–120 m a.s.l.),
154 characterize the heavily urbanized and industrialized core of the Beijing–Tianjin–
155 Hebei megacity cluster. The Wangdu (WD) site in suburban Baoding represents
156 regional background conditions, whereas the Shijiazhuang Luancheng (SJZ_LC) site
157 was included to better resolve pollution features specific to industrial cities. The
158 Shanxi University (SXU) site in the Taihang Mountains (780 m a.s.l.) provides critical
159 constraints on pollutant formation and transport between mountainous terrain and
160 adjacent plains. In East China, stations are distributed across the Yangtze River Delta
161 and its hinterland, covering topography from coastal lowlands to inland mountains.
162 The summit of Mount Tai (TS; 1,500 m a.s.l.) offers vertical profiles under relatively
163 clean, high-altitude background conditions. The Nanjing University of Information
164 Science and Technology (NUIST) site represents a densely populated and
165 economically developed urban environment, while sites at Huaibei Normal University
166 (HNU), Anhui University (AHU), and Changfeng (CF) in Anhui Province (30–35 m
167 a.s.l.) capture urban–suburban transition regimes. Southwest China is represented by
168 the Chengdu Academy of Environmental Sciences (CDAES; 505 m a.s.l.) on the
169 Chengdu Plain and the Chongqing (CQ; 332 m a.s.l.) site within the Sichuan Basin.
170 These stations are strategically located to investigate pollutant accumulation and
171 transport under high-humidity conditions and strong topographic confinement, and to
172 probe photochemical processes in complex terrain. In South China, a dense network
173 was established over the Pearl River Delta megacity region. In addition to sites at the
174 Guangzhou Institute of Geochemistry (GIG) and the Southern University of Science
175 and Technology (SUST) in Shenzhen, multiple stations in Guangzhou (Zhuliao,
176 Nansha, Timian, Gongyuan, and Daxuecheng; 15–155 m a.s.l.) form an intra-urban
177 array. This configuration allows detailed examination of the combined influences of
178 land–sea breezes, anthropogenic emissions, and local meteorology on the vertical
179 distributions of HONO and O₃. Central China is represented by the Luoyang (LY) site,
180 located in the middle reaches of the Yellow River within a mixed industrial–
181 agricultural region, providing key constraints on regional transport and accumulation
182 over the central plains. Together, the broad geographic coverage and pronounced
183 contrasts in elevation and surface type make this network well suited to resolve the
184 vertical distributions of aerosols, HONO, and O₃ across urban, suburban, coastal,
185 mountainous, and basin environments. It thus offers a robust observational basis for
186 investigating the dynamics of photochemical air pollution over major regions of
187 China.

188 Table 1. Geographic information of the stations in the Chinese Hyperspectral Ground-
189 Based Vertical Remote Sensing Network.

Region	Site (code)	Longitude (° E)	Latitude (° N)	Altitude (m)
--------	-------------	--------------------	-------------------	-----------------

North China	Chinese Academy of Meteorological Sciences (CAMS1)	116.32	39.94	100
	Chinese Academy of Meteorological Sciences (CAMS2)	116.32	39.94	100
	University of Chinese Academy of Sciences (UCAS)	116.67	40.4	120
	Wangdu (WD)	115.15	38.17	35
	Shijiazhuang_Luancheng (SJZ_LC)	114.61	37.91	70
	Shanxi University (SXU)	112.58	37.63	780
East China	Taishan (TS)	117.1	36.25	1500
	Nanjing University of Information Science and Technology (NUIST)	118.71	32.2	73
	Lin'an (LA)	119.75	30.3	140
	Huaibei Normal University (HNU)	116.8	33.98	35
	Anhui University (AHU)	117.18	31.77	30
Southwest China	Changfeng (CF)	117.18	32.21	30
	Chengdu Academy of Environmental Sciences (CDAES)	104.04	30.65	505
South China	Chongqing (CQ)	106.5	29.6	332
	Guangzhou Institute of Geochemistry (GIG)	113.35	23.15	30
	Southern University of Science and Technology (SUST)	113.99	22.59	40
	Guangzhou_Zhuliao (GZ_ZL)	113.34	23.36	20
	Guangzhou_Nansha (GZ_NS)	113.61	22.77	15
	Guangzhou_Timian (GZ_TM)	113.29	23.55	155
	Guangzhou_Gongyuan (GZ_GY)	113.26	23.13	15
	Guangzhou_Daxuecheng (GZ_DXC)	113.39	23.04	10
Central China	Luoyang (LY)	112.45	34.67	100

190
191
192
193
194
195
196
197
198
199
200
201
202
203
204
205
206
207
208
209
210

2.2 Instrument setup

Between 2021 and 2024, the 22 stations were operated during different periods using a standardized instrument configuration comprising a telescope, a spectrometer, and a control computer. The telescope consisted of a right-angle prism and a plano-convex lens with a [full](#) field of view $<0.3^\circ$, and was mounted on motorized stages that independently controlled elevation and azimuth angles, enabling multi-directional measurements of atmospheric constituents. The spectrometer covered the ultraviolet (296–408 nm) and visible (420–565 nm) wavelength ranges, while the computer handled instrument control and spectral data acquisition. All sites employed an identical elevation scanning sequence of 1° , 2° , 3° , 4° , 5° , 6° , 8° , 10° , 15° , 30° , and 90° (Liu et al., 2022a; Xing et al., 2021a, 2023). The integration time at each elevation [angle](#) was 1 min, [yielding a full scan cycle of approximately 12 min, which is the total time to complete all elevation measurements and be ready to initiate the next scanning cycle](#) yielding a full scan cycle of ~ 12 min. Routine measurements were conducted during daytime (08:00–18:00 local time). [For instrument calibration purposes only, the instruments operated at night to record dark current and electronic offsets.](#) ~~The instruments also operated at night to record dark current and electronic offsets, which were subsequently applied in the spectral calibration.~~ To minimize stratospheric contamination, [daytime](#) spectra acquired at solar zenith angles greater than 75° were excluded from further analysis.

设置了格式: 字体颜色: 文字 1

211
212
213
214
215
216
217
218
219
220
221
222
223
224
225
226
227
228
229
230

2.3 Spectral retrieval

Ultraviolet–visible spectra measured by the ground-based instruments were analysed with the QDOAS software ([version 3.2](#)) developed by BIRA-IASB. Differential optical absorption spectroscopy (DOAS) was applied to retrieve the differential slant column densities (DSCDs) of the oxygen dimer (O₄), O₃, and HONO. For each elevation scan, the zenith spectrum (90° elevation) [acquired within the same scanning sequence](#) was used as the reference and subtracted from spectra at lower elevation angles, thereby isolating the narrow-band absorption features of trace gases from broadband structures and enabling robust retrieval of target species. The fitting settings follow Xing et al. (2021, 2024a, b) and are summarized in Table 2. To account for the Ring effect arising from rotational Raman scattering and Fraunhofer line filling-in, a Ring spectrum calculated with DOASIS was included in the fit. Broadband spectral structures were represented and removed using a fifth-order polynomial. [This](#) allowing accurate separation of narrow-band molecular absorption. Strict quality control was applied: only retrievals with a root-mean-square (RMS) fitting residual below 1×10^{-3} were retained, ensuring the robustness and stability of the dataset. Representative spectral fits and residuals for O₄, O₃, and HONO are shown in Figure 1.

Table 2. Detailed retrieval settings for O₄, O₃, and HONO.

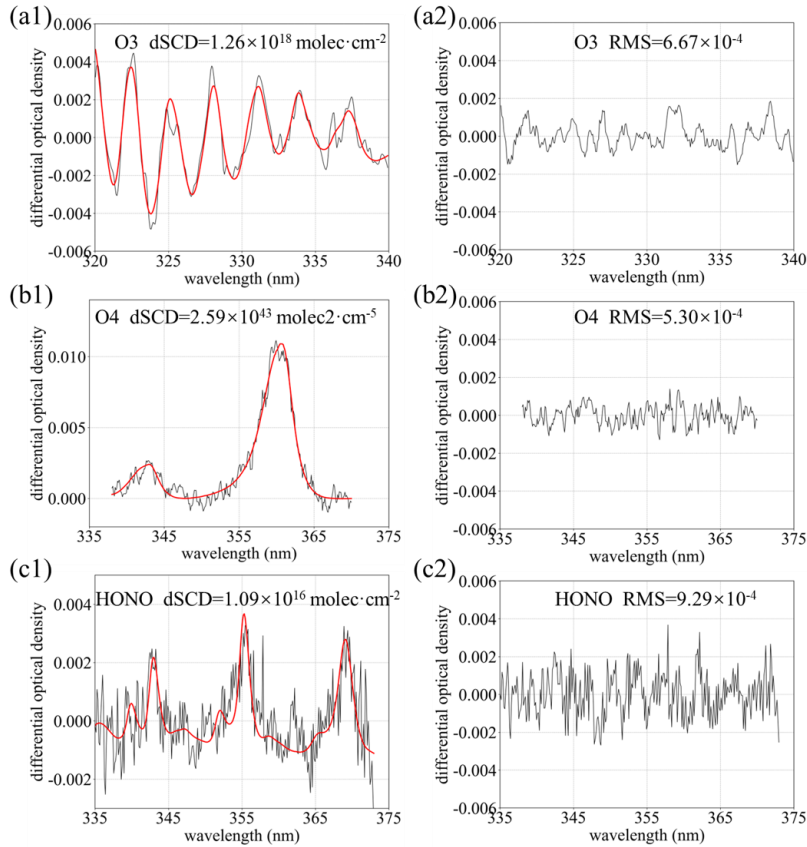
Parameter	Data source	Fitting interval		
		O ₄	O ₃	HONO
Wavelength range		338–370 nm	320–340 nm	335–373 nm
NO ₂	220 K, I ₀ * correction (SCD of 10^{17} molec·cm ⁻²); (Vandaele et al., 1998)	√	×	√
NO ₂	298 K, I ₀ correction (SCD of 10^{17} molec·cm ⁻²); (Vandaele et al., 1998)	√	√	√
O ₃	223 K, I ₀ correction (SCD of 10^{18} molec·cm ⁻²); (Serdyuchenko et al., 2014)	√	√	√
O ₃	243 K, I ₀ correction (SCD of 10^{18} molec·cm ⁻²); (Serdyuchenko et al., 2014)	×	×	√
O ₃	293 K, I ₀ correction (SCD of 10^{18} molec·cm ⁻²); (Serdyuchenko et al., 2014)	√	√	×
O ₄	293 K, I ₀ correction (SCD of 3×10^{43} molec ² ·cm ⁻⁵); (Thalman and Volkamer, 2013)	√	√	√
HCHO	293 K, I ₀ correction (SCD of 5×10^{15} molec·cm ⁻²); (Orphal and Chance, 2003)	√	√	√
BrO	273 K, I ₀ correction (SCD of 10^{13} molec·cm ⁻²); (Fleischmann et al., 2004)	√	×	√
Ring	Ring spectra calculated with DOASIS	√	√	√

格式化表格

格式化表格

	I ₀ correction			
HONO	(SCD of 10 ¹⁵ molec·cm ⁻²); (Stutz et al., 2000)	×	×	√
Polynomial degree		5	5	5
Intensity offset		Constant	Constant	No

231 * Solar I₀ correction, Aliwell et al.(2002).



232
233 Figure 1. (a1) O₃, (b1) O₄, and (c1) HONO DOAS fitting examples; (a2) O₃, (b2) O₄,
234 and (c2) HONO fitting residuals.

235

236 2.4 Vertical profile retrieval algorithm

237 Vertical profiles of aerosols and trace gases (HONO and O₃) were retrieved using
238 an inversion framework based on the optimal estimation method (OEM). The forward
239 radiative transfer calculations were performed with the linearized pseudo-spherical
240 vector discrete ordinate model VLIDORT (Spurr, 2006). The posterior state vector \mathbf{x}
241 was obtained by minimizing the cost function χ^2 :

$$242 \chi^2 = (\mathbf{y} - \mathbf{F}(\mathbf{x}, \mathbf{b}))^T \mathbf{S}_\epsilon^{-1} (\mathbf{y} - \mathbf{F}(\mathbf{x}, \mathbf{b})) + (\mathbf{x} - \mathbf{x}_a)^T \mathbf{S}_a^{-1} (\mathbf{x} - \mathbf{x}_a) \quad (1)$$

243 where y denotes the measured DSCDs, $F(x, b)$ is the forward model, b represents
244 ancillary meteorological parameters (e.g., temperature, pressure, single-scattering
245 albedo, and asymmetry factor), x_a is the a priori state vector, S_e is the measurement
246 error covariance matrix, and S_a is the a priori covariance matrix. For both aerosols
247 and trace gases, the a priori vertical profiles were assumed to decrease exponentially
248 with altitude, reflecting the characteristic rapid decay of pollutant concentrations
249 within the planetary boundary layer. Because the absorption of the O_4 is strongly
250 linked to aerosol optical properties, aerosol vertical profiles were first retrieved from
251 multi-elevation O_4 DSCDs and subsequently used as inputs to the forward model for
252 the retrieval of O_3 and HONO profiles. The atmosphere from the surface to 4 km was
253 discretized into 20 layers with a vertical resolution of 200 m (Xing et al., 2024b).
254 Retrievals were subjected to strict quality control: profiles with degrees of freedom
255 (DOF) below 1.0, χ^2 values exceeding 200, or relative uncertainties greater than 50%
256 were excluded from further analysis.

257

258 **2.5 TUV model**

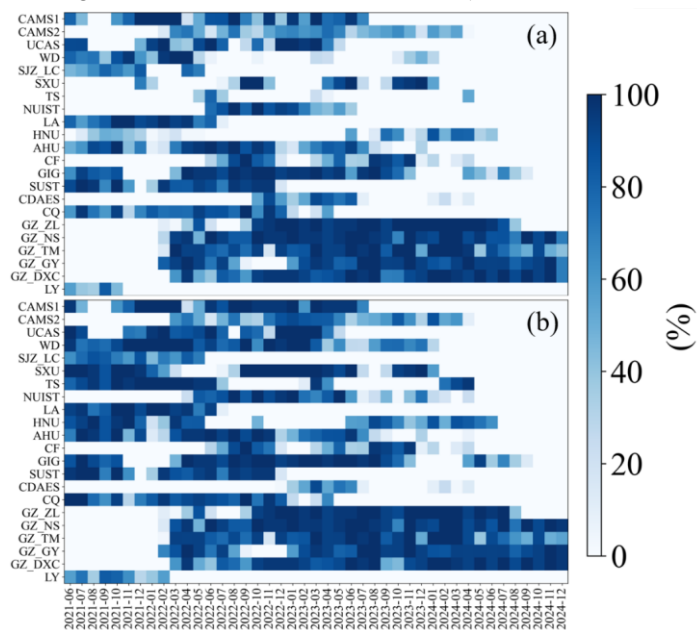
259 Photolysis rates of HONO and O_3 were computed with the Tropospheric
260 Ultraviolet and Visible (TUV) radiative transfer model developed by NCAR, which is
261 based on rigorous radiative transfer theory and implemented in FORTRAN
262 (<https://www2.acom.ucar.edu/modeling/tropospheric>, last access: 26 January 2026).
263 The TUV model simulates the propagation of solar radiation in the troposphere under
264 prescribed optical and chemical conditions and provides spectrally resolved
265 photolysis frequencies for key atmospheric reactions. These rates were used to
266 quantify the contributions of HONO and O_3 photolysis to OH production. Model
267 inputs included AOD at ~ 361 nm derived from MAX-DOAS-retrieved aerosol
268 extinction profiles, total ozone column from daily TROPOMI observations (typically
269 260–280 DU), and single-scattering albedo (SSA) constrained by regression analyses
270 of O_4 absorptions at 361 and 477 nm (Xing et al., 2019).

271

272 **3. Vertical profile observations of atmospheric composition**

273 Figure 2 summarizes the monthly completeness of O_3 and HONO vertical profile
274 measurements at 22 sites from 2021 to 2024. Shading denotes the fraction of valid
275 observations, with 100% indicating uninterrupted daytime measurements and
276 successful profile retrievals throughout the month. Because stations were
277 commissioned at different times and operated under varying maintenance and field
278 conditions, the available observation periods differ among sites. Most stations provide
279 long, continuous time series of both HONO and O_3 . More than 85% of the sites had
280 operational histories spanning over one year, and 60% for more than two years,
281 although these periods may include intermittent data gaps due to maintenance,
282 weather, or technical issues, with only quality-controlled valid profiles retained in the
283 dataset~~More than 85% of the sites operated for over one year, and 60% for more~~
284 ~~than two years~~, demonstrating the temporal stability of the network. This coverage

285 enables robust characterization of seasonal and diurnal variability under diverse
 286 climatic regimes and emission backgrounds. Although a few sites had shorter
 287 operational periods owing to instrument commissioning and field constraints, they
 288 still delivered several months of continuous high-quality data, which are valuable for
 289 regional intercomparison and support analyses of long-term trends and photochemical
 290 processes. Isolated months with missing or incomplete data occur at some sites,
 291 primarily because of unavoidable factors such as instrument maintenance, power
 292 interruptions, persistent cloud or precipitation, and quality-control filtering (e.g.,
 293 excessive fitting residuals or low DOF in the retrievals).



294
 295 Figure 2. Monthly data completeness of the vertical profiles of (a) O_3 and (b) HONO.
 296

297 3.1 HONO

298 Figure 3 presents the 2021–2024 mean vertical profiles of HONO across all sites.
 299 At every location, HONO is strongly enriched near the surface and decreases rapidly
 300 with height, following an approximately exponential decay. This structure is
 301 characteristic of a boundary-layer-dominated species controlled by ground-based
 302 sources (Li et al., 2025b; Meng et al., 2020; Xing et al., 2024c; Xu et al., 2021). Peak
 303 mixing ratios occur within the lowest 0–0.5 km, decline sharply between 0.5 and 1.5
 304 km, and generally fall to regional background or near the detection limit above 2 km
 305 (<0.05 – 0.1 ppb), becoming negligible by 4 km. Such steep gradients reflect dominant
 306 near-surface emissions and nocturnal heterogeneous formation of HONO from NO_2
 307 on ground and aerosol surfaces, combined with its short photochemical lifetime and
 308 rapid daytime photolysis, which preclude sustained accumulation in the free

309 troposphere (Li et al., 2025b; Meng et al., 2020; Xing et al., 2024a). Pronounced
310 regional contrasts are evident. Urban sites in North and East China (e.g., CAMS1,
311 CAMS2, WD, SXU, AHU) exhibit the highest near-surface HONO (0.3–0.5 ppb
312 below 0.3 km), followed by a rapid decrease to <0.1 ppb above 1 km. The sharp
313 vertical gradients and absence of secondary maxima aloft indicate strong control by
314 surface sources and nocturnal heterogeneous production, with efficient removal by
315 turbulent mixing and photolysis within the planetary boundary layer (Xu et al., 2021).
316 In contrast, background or relatively clean sites (e.g., TS, LA) show much lower
317 concentrations, with near-surface values typically <0.2 ppb and a monotonic decrease
318 with altitude, consistent with weak local emissions and dominance of regional
319 background (Garcia-Nieto et al., 2018b; Li et al., 2025b). Sites in South and
320 Southwest China (e.g., GZ_ZL, GZ_NS, GZ_DXC, CQ, CDAES) display a similar
321 monotonic decay: elevated HONO confined to the lowest 0–0.5 km and rapid
322 attenuation to background levels above 1–2 km, without a ~~distinct~~^{persistent} mid-level
323 enhancement. Although near-surface mixing ratios at some locations (e.g., GZ_DXC,
324 CQ) approach or slightly exceed 0.3 ppb, their vertical decay rates are comparable to
325 those at northern and eastern urban sites. This indicates that, even under high
326 humidity or complex topography, HONO remains largely restricted to the lower
327 boundary layer, governed by its short lifetime, fast photolysis, and dilution by
328 convective mixing, while large-scale vertical transport contributes little to its
329 maintenance aloft (Li et al., 2025b; Xing et al., 2021b; Xu et al., 2021). Seasonal
330 mean profiles are shown in Figures S1–S4. Taken together, the regionally averaged
331 profiles consistently demonstrate strong near-surface accumulation and rapid vertical
332 attenuation of HONO. This confirms that HONO is a short-lived, boundary-layer-
333 derived reactive nitrogen species, tightly coupled to surface emissions and
334 heterogeneous chemistry. It therefore plays a key role in initiating early-morning OH
335 production and regulating boundary-layer oxidizing capacity, whereas its direct
336 impact in the free troposphere is comparatively minor.

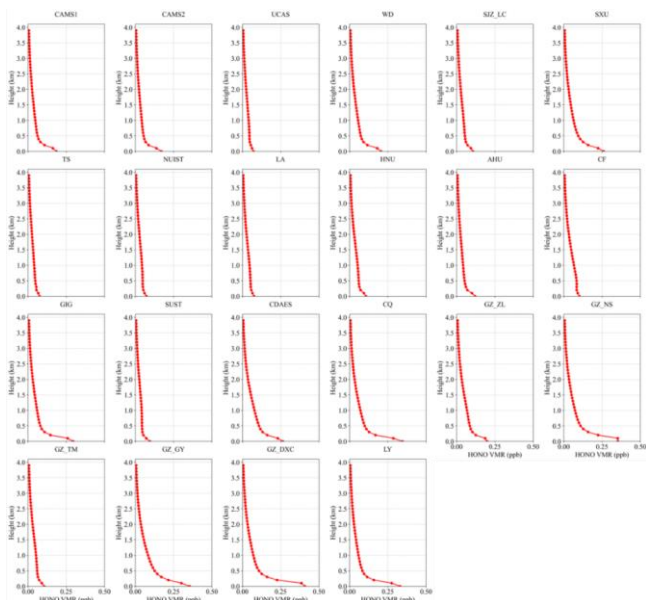


Figure 3. Mean vertical profiles of HONO averaged over 2021–2024.

337
338
339
340
341
342
343
344
345
346
347
348
349
350
351
352
353
354
355
356
357
358
359
360
361

Figure 4 illustrates the mean diurnal evolution of HONO. As a key reactive nitrogen species, HONO exhibits vertical and temporal patterns that integrate the effects of surface emissions, heterogeneous and photochemical processes, and boundary-layer dynamics. Based on HONO data obtained from the hyperspectral vertical remote-sensing network, pronounced regional and site-specific patterns are observed. Across North China (CAMS1, CAMS2, UCAS, WD, SJZ_LC and SXU), HONO exhibits a clear near-surface morning maximum followed by an afternoon minimum. At CAMS1 and CAMS2, the 0–1 km volume mixing ratio (VMR) peaks at 08:00–10:00 local time (0.3–0.4 ppb) and decreases to 0.1–0.2 ppb by 14:00–16:00. This pattern reflects nocturnal accumulation driven by heterogeneous conversion of NO_2 on aerosol and ground surfaces (Liu et al., 2022a; Xing et al., 2023; Xuan et al., 2025b), and, after sunrise, enhanced solar radiation leads to the release and photochemical processing of HONO; meanwhile, morning rush-hour emissions of NO_2 and VOCs further promote HONO formation (Garcia-Nieto et al., 2018a; Zhang et al., 2025a). At the mountain site SXU, topography-induced temperature inversions enhance nighttime accumulation, yielding a more pronounced morning peak. In contrast, UCAS and WD, characterized by weaker anthropogenic emissions, show lower near-surface HONO levels and smaller diurnal amplitudes. In East China (TS, NUIST, LA, HNU, AHU and CF), urban sites display modest morning enhancements (0.2–0.3 ppb at 08:00–10:00) followed by afternoon decreases driven by boundary-layer growth and photolysis. At the high-altitude TS site (1500 m), HONO remains below 0.1 ppb with weak diurnal variability, reflecting clean background conditions and efficient vertical mixing. Sites with dense vegetation or agricultural land use (LA

设置了格式: 下标

362 and CF) may receive contributions from biogenic VOC-related chemistry, but the
363 overall pattern still features a subdued morning maximum(Liang et al., 2017; Ryan et
364 al., 2018a; Xue et al., 2021; Ye et al., 2023a). At South China and Southwest China
365 sites (GIG, SUST, CDAES, CQ and the Guangzhou cluster: GZ_ZL, GZ_NS,
366 GZ_TM, GZ_GY and GZ_DXC), warm and humid conditions together with basin or
367 coastal circulations further modulate the diurnal cycle. Urban stations typically reach
368 0.3–0.5 ppb near the surface in the morning and decline to 0.1–0.2 ppb in the
369 afternoon. In the Sichuan Basin (CQ), strong nocturnal inversions favour HONO
370 accumulation, producing slightly higher morning peaks (0.4–0.5 ppb). At coastal sites,
371 land–sea breeze circulation leads to a transient morning enhancement followed by
372 dilution by cleaner marine air masses. At the Central China site LY, the diurnal pattern
373 resembles that in North and South China, with a clear morning maximum and lower
374 concentrations in the afternoon associated with boundary-layer development.
375 Seasonal mean diurnal vertical profiles are shown in Figures S5–S8. Overall, the
376 diurnal cycle of HONO is governed by three coupled processes: (i) nocturnal
377 heterogeneous production from NO₂ on aerosol and surface substrates, which drives
378 early-morning maxima (Li et al., 2025b; Meng et al., 2020; Xuan et al., 2024); (ii)
379 enhancement by morning anthropogenic emissions of NO_x and VOCs from traffic and
380 industrial activities (Hao et al., 2020; Zhang et al., 2025a, 2023b); and (iii) rapid
381 photolysis and boundary-layer dilution in the afternoon (Xing et al., 2021b, 2024a;
382 Zhang et al., 2023b). Regional contrasts arise from the combined effects of emission
383 intensity, topography (basin, mountain and coastal settings), and meteorological
384 conditions, particularly temperature inversions and ventilation efficiency (Li et al.,
385 2025b; Xuan et al., 2024; Zhang et al., 2025a).

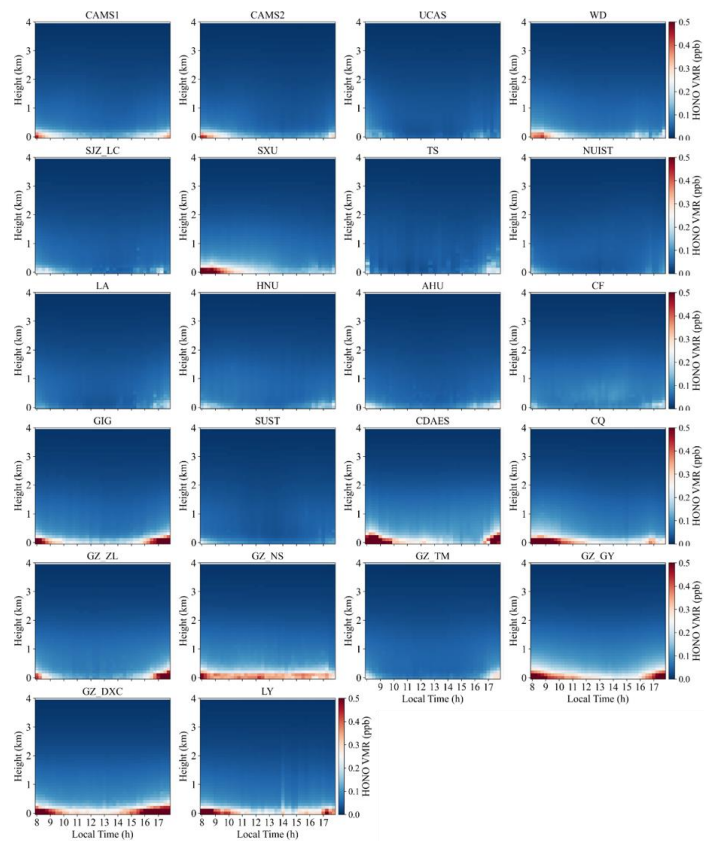


Figure 4. Mean diurnal vertical profiles of HONO for 2021–2024.

386

387

388

389 3.2 O₃

390

391

392

393

394

395

396

397

398

399

400

401

402

Figure 5 presents the mean vertical profiles of O₃ averaged over 2021–2024 for all sites. A consistent “low near the surface–high aloft” structure is observed, characterized by a monotonic increase or a weak S-shaped pattern. O₃ VMR are lowest in the lowest 0–0.5 km (20–60 ppb), rise rapidly between 1 and 2 km, and reach daytime maxima at 3–4 km (60–100 ppb). This vertical gradient agrees well with MAX-DOAS and ozone-sonde observations over eastern China and other regions worldwide (Couillard et al., 2021; Ji et al., 2023; Liao et al., 2024; Su et al., 2017; Wang et al., 2018; Zeng et al., 2023), and reflects the combined effects of strong near-surface NO₂ titration, dry deposition, and boundary-layer mixing that suppress O₃, together with photochemical production and regional transport that enhance O₃ aloft (Couillard et al., 2021; Donzelli and Suarez-Varela, 2024; Liao et al., 2024; Zeng et al., 2023; Zhu et al., 2025b). Within the boundary layer (0–1 km), O₃ generally increases sharply with height, and a weak local maximum or inflection is

403 often found at 0.2–0.5 km. This contrasts with the vertical distributions of NO₂ and
404 HCHO at the same sites, which show high near-surface concentrations dominated by
405 emissions (Couillard et al., 2021; Hu et al., 2024; Hong et al., 2022; Jiao et al., 2025;
406 Liu et al., 2023b). In contrast, O₃ is efficiently removed near the ground by nocturnal
407 NO₂ titration and daytime surface deposition (Liao et al., 2024; Xing et al., 2022). At
408 urban and suburban stations (e.g., UCAS and CF), O₃ in the lowest 0–0.3 km can
409 decrease to 20–40 ppb, indicating strong titration by traffic and industry related NO₂
410 (Hu et al., 2024). Between 1 and 3 km, O₃ increases nearly monotonically at most
411 sites, with the largest vertical gradient typically occurring around 2–3 km. This layer
412 often corresponds to the daytime boundary-layer top or the nocturnal residual layer
413 and represents a key altitude for regional photochemical accumulation and downward
414 transport (He et al., 2023b; Liao et al., 2024; Zhu et al., 2025a). Numerous studies
415 have shown that O₃-rich air in the upper boundary layer and residual layer can be
416 mixed downward during boundary-layer growth, and that O₃ stored aloft at night is re-
417 entrained to the surface the following morning, making an important contribution to
418 surface O₃ levels (Ancellet et al., 2024; Donzelli and Suarez-Varela, 2024; Liu et al.,
419 2022b; Shi et al., 2022; Song et al., 2024; Wang et al., 2024b). At 3–4 km, O₃ VMR
420 further increase and tend to level off, with some sites exhibiting distinct maxima. At
421 these altitudes, the influence of surface NO₂ titration becomes negligible, whereas
422 long-range transport and possible stratosphere–troposphere exchange start to play a
423 role. Previous studies have shown that enhanced O₃ at 3–5 km over East Asia in
424 spring and summer can partly arise from stratospheric intrusions and westerly long-
425 range transport (Li et al., 2025a; Liao et al., 2024, 2025; Park et al., 2020). The
426 pronounced O₃ enhancements observed at 3–4 km at sites such as CQ, GZ_TM and
427 [SUIST-SUST](#) are therefore likely linked to free-tropospheric background O₃ and
428 regional-scale transport processes. Seasonal mean O₃ vertical profiles are shown in
429 Figures S9–S12.

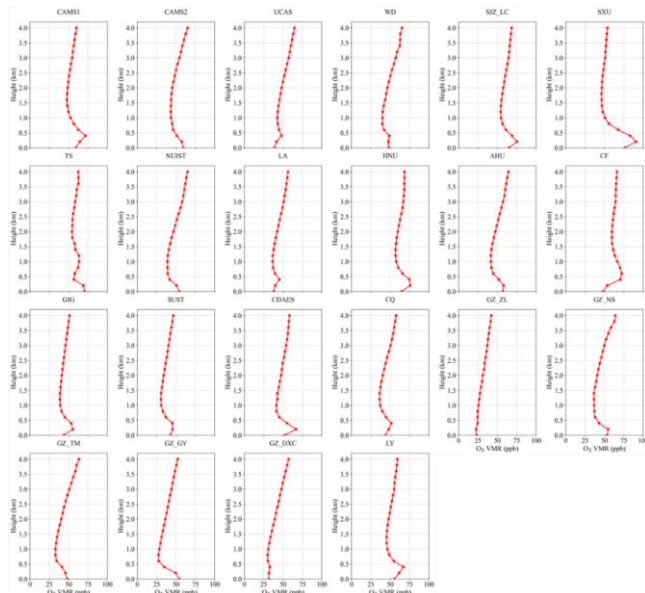


Figure 5. Mean vertical profiles of O₃ averaged over 2021–2024.

430
431

432

433

434

435

436

437

438

439

440

441

442

443

444

445

446

447

448

449

450

451

452

453

454

Figure 6 presents the mean diurnal evolution of O₃. All sites exhibit pronounced daily cycles with clear regional contrasts. O₃ typically peaks in the morning (08:00–10:00) or in the early afternoon (12:00–15:00), in phase with the diurnal variation of solar irradiance and photochemical reaction rates (Xia et al., 2021; Yang et al., 2020). This behaviour is most evident in North and East China, whereas the cycle is weaker in South China, likely owing to persistently high temperature and humidity that modulate boundary-layer development and photochemistry (Zhou et al., 2022). At several sites (e.g., TS, CDAES and CQ), enhanced O₃ at 1–2 km during 12:00–15:00 points to the influence of local meteorology and emission distributions (Chen et al., 2023; Li et al., 2025a). In contrast, morning maxima at CAMS1, CAMS2, UCAS, NUIST and AHU reflect the rapid re-entrainment and photochemical processing of O₃ accumulated overnight after sunrise (David and Nair, 2011; Liao et al., 2023). The vertical structure of the diurnal cycle also differs markedly among regions. North China sites show strong near-surface variability, whereas peak O₃ in South China is generally lower, consistent with regional differences in pollution levels and meteorological conditions. Relatively high near-surface O₃ at GZ_ZL and GZ_NS is likely linked to local emissions combined with weak dispersion (Yang et al., 2020; Zhou et al., 2022). North China stations (CAMS1, CAMS2, UCAS, WD, SJZ_LC and SXU) display a typical urban O₃ diurnal pattern. At CAMS1 and CAMS2, O₃ in the 0–1 km layer reaches 80–120 ppb in the morning (08:00–10:00) and decreases markedly in the early afternoon, reflecting rapid boundary-layer growth and photochemical loss after sunrise (David and Nair, 2011; Liao et al., 2023). UCAS and WD show similar morning maxima, whereas SJZ_LC is characterized by lower and

455 more stable O₃, indicative of relatively clean background conditions. At SXU, high
456 morning O₃ (80–100 ppb) is followed by even higher afternoon levels (>100 ppb),
457 pointing to strong in situ secondary production under intense photochemical activity
458 (Wang et al., 2017; Xia et al., 2021). East China sites (TS, NUIST, LA, HNU, AHU
459 and CF) exhibit more complex diurnal behaviour. At TS, O₃ peaks at 1–2 km during
460 12:00–15:00 (80–100 ppb), suggesting an important role of vertical transport and
461 local emissions. NUIST and AHU show morning maxima similar to those in North
462 China, whereas LA maintains low and weakly varying O₃, consistent with relatively
463 clean conditions (Chen et al., 2024). At HNU, near-surface O₃ increases in the early
464 afternoon (60–80 ppb), reflecting active photochemistry (Wang et al., 2025c). CF
465 shows a pronounced afternoon peak (13:00–17:00, 80–120 ppb), indicating a strong
466 influence of local sources (Xia et al., 2021; Yang et al., 2020). South China sites (GIG,
467 SUST, GZ_ZL, GZ_NS, GZ_TM, GZ_GY and GZ_DXC) differ substantially from
468 those in the north and east. GIG exhibits low and weakly varying O₃, representative of
469 background conditions (Chen et al., 2024; Lin et al., 2022). The other sites show
470 morning near-surface maxima (80–100 ppb at 08:00–10:00), followed by decreases
471 associated with rapid boundary-layer development after sunrise (David and Nair, 2011;
472 Liao et al., 2023), and enhanced O₃ at 3–4 km in the afternoon (13:00–17:00),
473 highlighting the pronounced vertical structure of O₃ pollution in this region.
474 Southwestern sites (CDAES and CQ) display distinct afternoon enhancements at 1–2
475 km. At CDAES, O₃ reaches 80–120 ppb during 15:00–18:00, likely favored by high
476 temperature and humidity that accelerate photochemical production (Yang et al., 2020;
477 Zhang et al., 2022), while CQ shows a similar but weaker enhancement (60–80 ppb).
478 The central China site LY exhibits morning near-surface maxima (60–80 ppb) and
479 elevated O₃ at 2–4 km in the afternoon, characteristic of a typical urban diurnal cycle.
480 Seasonal mean diurnal vertical profiles are shown in Figures S13–S16. These regional
481 contrasts underline the differing controls on O₃ across China, with strong local
482 photochemistry in North China, combined regional transport and sustained
483 photochemical production in South China, and mixed influences of emissions and
484 meteorology in East China.

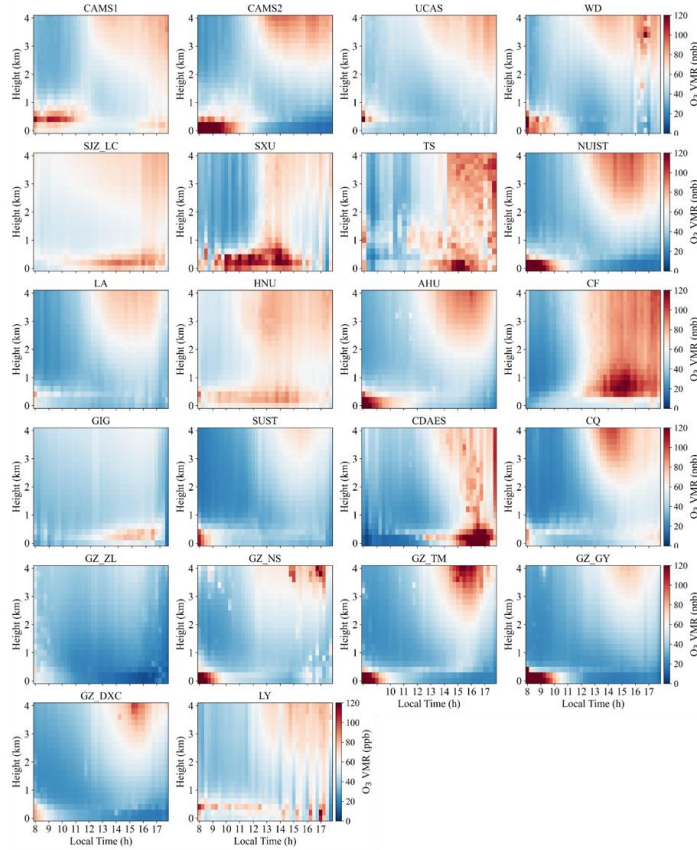


Figure 6. Mean diurnal vertical profiles of O_3 for 2021–2024.

3.3 OH production

Photolysis of HONO and O_3 constitutes a primary source of OH radicals and therefore controls the atmospheric oxidation capacity (AOC). To quantify the AOC at each site, we evaluated altitude-resolved OH production from HONO and O_3 using [retrieved in situ concentration](#) profiles combined with photolysis frequencies calculated by the TUV model. OH production from HONO and O_3 was computed from the following expressions.

$$P(OH)_{HONO} = J(HONO) \times [HONO] \quad (2)$$

$$P(OH)_{O_3} = 2 \times f \times J(O(^1D)) \times [O_3] \quad (3)$$

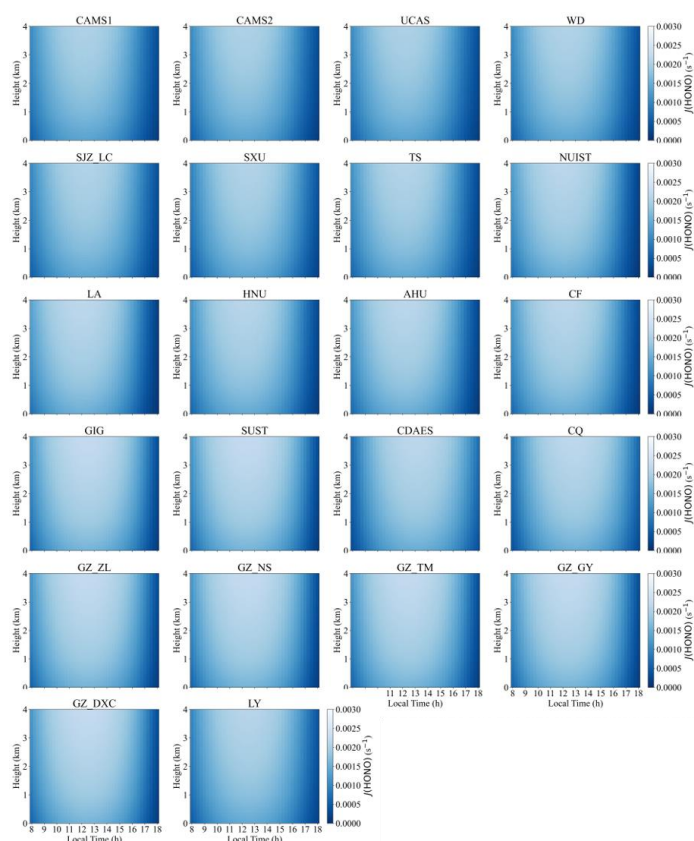
Here, $J(HONO)$ and $J(O(^1D))$ are the photolysis rate coefficients of HONO and O_3 , respectively, obtained from the TUV model. $O(^1D)$ denotes electronically excited atomic oxygen produced by O_3 photodissociation, and f represents the branching

带格式的：居中

500 fraction of the reaction $O(^1D) + H_2O \rightarrow 2OH$. [HONO] and [O₃] are the
501 concentrations of HONO and O₃ at each altitude level.

502 Figure 7 presents the mean diurnal vertical profiles of the HONO photolysis
503 frequency, J(HONO), at 22 sites during 2021–2024; the corresponding seasonal mean
504 diurnal variations are presented in Figures S17–S20. All sites exhibit a canonical
505 photochemical pattern: J(HONO) increases rapidly after sunrise, reaches a maximum
506 around local noon, and then gradually decreases with increasing solar zenith angle.
507 Elevated values persist between 10:00 and 14:00 local time, with peak J(HONO)
508 typically occurring near 12:00–13:00, indicating that HONO photolysis is primarily
509 controlled by solar irradiance, in agreement with observations in Beijing and
510 Guangzhou (He et al., 2023c; Ryan et al., 2018b). Vertically, J(HONO) increases
511 systematically with altitude. Photolysis rates are relatively low in the near-surface
512 layer (0–0.5 km), increase markedly in the upper mixed layer and lower free
513 troposphere (approximately 1–3 km), and reach maxima between 2 and 4 km, with
514 peak values around $2.5 \times 10^{-3} \text{ s}^{-1}$. This “weaker near the surface and stronger aloft”
515 structure is highly consistent with the J(HONO) profiles reported by Xing et al.
516 (2024a) and reflects the combined effects of aerosol attenuation of ultraviolet
517 radiation in the lower atmosphere and enhanced shortwave actinic flux at higher
518 altitudes (He et al., 2023c; Ryan et al., 2018b; Spataro and Ianniello, 2014). At the
519 North China sites (CAMS1, CAMS2, UCAS, WD, SJZ_LC, SXU), J(HONO) exhibits
520 a pronounced diurnal cycle, increasing ~~after sunrise during the morning (08:00–10:00)~~
521 with rising solar radiation, peaking at midday (12:00–14:00) at 0.0020–0.0025 s⁻¹, and
522 decreasing in the afternoon (14:00–18:00). The urban Beijing sites CAMS1 and
523 CAMS2 show peak values of ~0.0025 s⁻¹, comparable to those at other North China
524 Plain stations (e.g., UCAS and WD), reflecting strong photolysis under high HONO
525 loading and favourable radiation conditions. At SJZ_LC, located at the foothills of the
526 Taihang Mountains, morning J(HONO) is slightly enhanced, likely owing to
527 temperature inversions that modulate the vertical distribution of aerosols and actinic
528 flux. The elevated site SXU (780 m a.s.l.) exhibits systematically higher J(HONO)
529 than lowland stations, with a peak of ~0.0022 s⁻¹, consistent with reduced aerosol
530 extinction and stronger solar radiation at higher altitude. East China sites (TS, NUIST,
531 LA, HNU, AHU, CF) display similar peak timing to North China but slightly lower
532 magnitudes (0.0015–0.0025 s⁻¹). For example, J(HONO) at NUIST peaks at ~0.0020
533 s⁻¹, whereas the high-altitude background site TS (1500 m a.s.l.) reaches ~0.0021 s⁻¹,
534 consistent with enhanced actinic flux under cleaner atmospheric conditions. In South
535 China (GIG, SUST, GZ_ZL, GZ_NS, GZ_TM, GZ_GY, GZ_DXC), the maximum
536 J(HONO) occurs slightly later in the day (13:00–15:00) and attains higher values
537 (0.0020–0.0030 s⁻¹). The highest peak is observed at GZ_DXC (~0.0030 s⁻¹), likely
538 reflecting elevated HONO concentrations promoted by warm and humid conditions
539 that favor heterogeneous formation. The southwestern basin site CQ shows a
540 comparable peak (~0.0025 s⁻¹), while the Central China site LY reaches ~0.0020 s⁻¹,
541 similar to values in North and East China. Overall, urban sites exhibit larger diurnal

542 amplitudes and 20–40% higher $J(\text{HONO})$ maxima than mountain or clean-
 543 background sites, owing to higher HONO abundances and aerosol loading that
 544 modulate the effective actinic flux. This behaviour is fully consistent with previous
 545 findings from Beijing, Shanghai and other megacities, which reported pronounced
 546 daytime enhancement of $J(\text{HONO})$ under high- NO_2 and high-HONO conditions (He
 547 et al., 2023c; Spataro and Ianniello, 2014; Ye et al., 2023b).



带格式的：居中

548

Figure 7. Mean diurnal vertical profiles of the HONO photolysis rate, $J(\text{HONO})$.

549

550

551

552

553

554

555

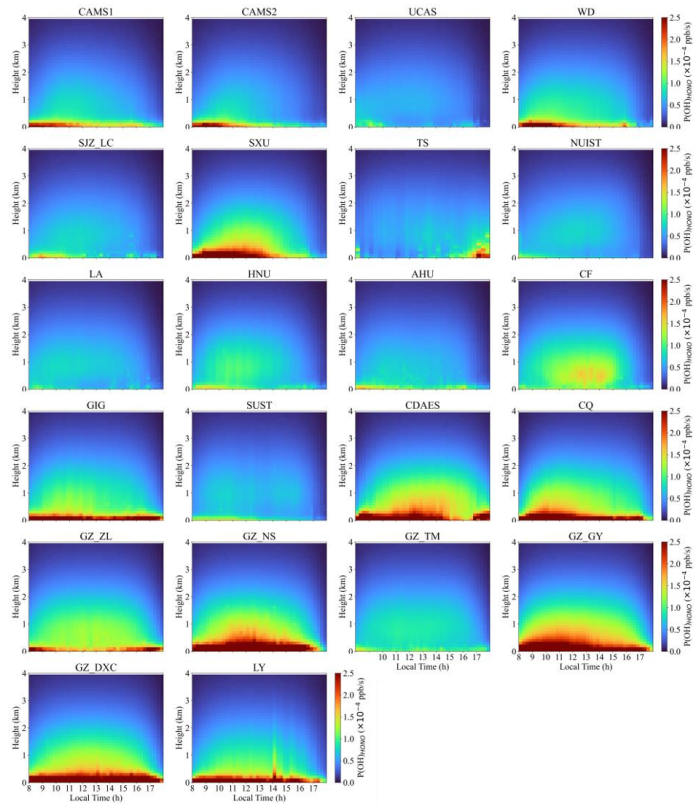
556

557

558

Figure 8 presents the mean diurnal vertical profiles of OH production from HONO photolysis, $P(\text{OH})_{\text{HONO}}$, at 22 sites; the corresponding seasonal mean profiles are shown in Figures S21–S24. At all sites, $P(\text{OH})_{\text{HONO}}$ displays a pronounced unimodal diurnal cycle, increasing rapidly after sunrise, peaking between 10:00 and 14:00, and declining thereafter. The peak timing closely follows the maximum of the $J(\text{HONO})$, whereas the peak altitude remains confined to the near-surface layer, reflecting the strong surface enhancement of HONO. In the lower boundary layer (0–0.5 km), $P(\text{OH})_{\text{HONO}}$ attains its column maximum, with most sites peaking between 11:00 and 13:00 and reaching 1.0×10^{-4} – 5.5×10^{-4} ppb·s⁻¹. For all stations,

559 P(OH)_{HONO} is largest within 0–1 km and decreases monotonically with height,
560 consistent with the preferential accumulation of HONO near the surface and the
561 resulting localization of photochemically produced OH (He et al., 2023c; Li et al.,
562 2025b; Xing et al., 2021b; Zhang et al., 2025a). Several sites, including SXU, CDAES,
563 CQ, GZ_NS, GZ_GY, and GZ_DXC, exhibit particularly strong OH production, with
564 peak P(OH)_{HONO} commonly exceeding 3.0×10^{-4} ppb·s⁻¹. This reflects the
565 combined effects of elevated HONO levels and intense solar radiation. At these
566 locations, the high- P(OH)_{HONO} layer can extend to 1–2 km, indicating a deeper
567 photochemically active region. This feature is consistent with earlier reports
568 highlighting the substantial contribution of HONO to OH in the lower free
569 troposphere (Aumont et al., 2003; R. Crilley et al., 2016; Xue et al., 2025; Zhang et al.,
570 2025a). Vertically, P(OH)_{HONO} decreases rapidly with altitude at all sites and is
571 reduced to 20–40% of its surface value above 2 km, demonstrating that the impact of
572 HONO photolysis on OH is largely confined to the boundary layer. In agreement with
573 previous observations in Beijing and Guangzhou (Gu et al., 2022; Meng et al., 2020;
574 Yu et al., 2022), HONO photolysis represents one of the dominant OH sources during
575 the morning and around local noon, accounting for 30–60% of the daytime OH
576 production near the surface (Song et al., 2023a; Tang et al., 2015). In the present study,
577 several plateau sites show even larger relative contributions at midday, indicating that
578 under conditions of low NO₂ and strong solar irradiance, HONO photolysis becomes
579 an especially efficient radical source, consistent with findings at Nam Co (Xing et al.,
580 2024b). Regionally, North China sites (CAMS1, CAMS2, UCAS, WD, SJZ_LC, and
581 SXU) exhibit near-surface (0–1 km) P(OH)_{HONO} maxima between 12:00 and 14:00
582 local time, with values of 1.0×10^{-4} – 3.0×10^{-4} ppb·s⁻¹. At CAMS1, the peak
583 reaches $\sim 1.5 \times 10^{-4}$ ppb·s⁻¹, whereas at SJZ_LC, although nocturnal temperature
584 inversions near the Taihang Mountains may favour HONO accumulation, the peak
585 remains modest ($\sim 1.2 \times 10^{-4}$ ppb·s⁻¹) owing to weaker local emissions,
586 comparable to UCAS and WD (1.0×10^{-4} – 2.5×10^{-4} ppb·s⁻¹). At these sites,
587 P(OH)_{HONO} declines sharply with height and is substantially reduced above 1 km,
588 underscoring the near-surface confinement of both HONO and [OH production from](#)
589 [its photolysis](#)~~its photolytic OH production~~. East China stations (TS, NUIST, LA,
590 HNU, AHU, and CF) show similar peak times (12:00–14:00) but slightly lower
591 magnitudes (1.0×10^{-4} – 1.5×10^{-4} ppb·s⁻¹). In South China (GIG, SUST, GZ_ZL,
592 GZ_NS, GZ_TM, GZ_GY, and GZ_DXC), peaks occur later (13:00–15:00) and are
593 substantially higher (2.5×10^{-4} – 5.5×10^{-4} ppb·s⁻¹), consistent with enhanced
594 heterogeneous HONO formation under warm and humid conditions. Southwest China
595 sites (CDAES and CQ) reach peak values of $\sim 3.5 \times 10^{-4}$ ppb·s⁻¹, comparable to
596 those in South China, likely owing to basin-induced HONO accumulation and
597 vigorous photochemistry. In Central China (LY), the peak ($\sim 2.7 \times 10^{-4}$ ppb·s⁻¹) is
598 similar to that in North and East China, indicating broadly comparable HONO sources
599 and photolysis efficiencies across these regions.



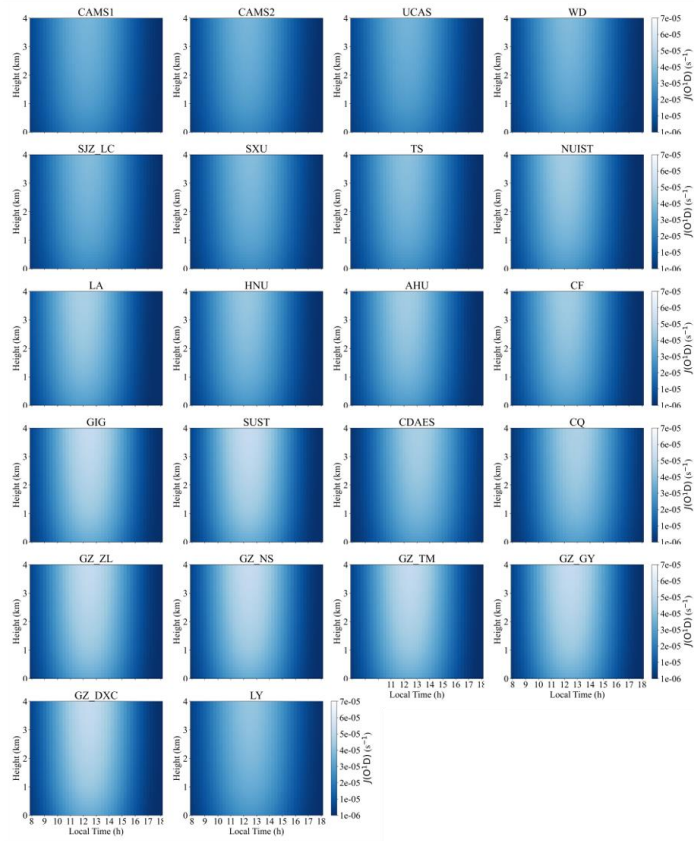
带格式的：居中

600

601 Figure 8. Mean vertical profiles of OH radicals generated by HONO photolysis.

602 Figure 9 presents the O_3 photolysis frequency, $J(O(^1D))$, at all 22 sites follows a
 603 pronounced diurnal cycle, with maxima consistently occurring between 12:00 and
 604 14:00 local time. Seasonal mean diurnal variations are presented in Figures S25–S28.
 605 In North China (CAMS1, CAMS2, UCAS, WD, SJZ_LC, and SXU), near-surface
 606 peak $J(O(^1D))$ ranges from $\sim 5 \times 10^{-5}$ to $7 \times 10^{-5} \text{ s}^{-1}$. The urban sites CAMS1, CAMS2,
 607 UCAS, and WD reach the highest values ($\sim 6 \times 10^{-5}$ – $7 \times 10^{-5} \text{ s}^{-1}$) at midday. At SJZ_LC,
 608 located at the foothills of the Taihang Mountains, nocturnal temperature inversions
 609 can favor O_3 accumulation (Guo et al., 2024b; He et al., 2021), but the peak remains
 610 slightly lower ($\sim 5 \times 10^{-5}$ – $6 \times 10^{-5} \text{ s}^{-1}$), likely constrained by local emissions. At the
 611 higher-altitude SXU site (780 m a.s.l.), near-surface $J(O(^1D))$ is reduced ($\sim 4 \times 10^{-5}$ –
 612 $5 \times 10^{-5} \text{ s}^{-1}$). Overall, urban stations exhibit larger $J(O(^1D))$ than suburban and rural
 613 sites, reflecting higher O_3 levels driven by anthropogenic precursors and consistent
 614 with reported regional contrasts (Fardilah et al., 2023; Guo et al., 2024a; Qiu et al.,
 615 2025). In East China (TS, NUIST, LA, HNU, AHU, and CF), near-surface $J(O(^1D))$
 616 peaks at $\sim 4 \times 10^{-5}$ – $6 \times 10^{-5} \text{ s}^{-1}$, with urban sites such as NUIST and AHU reaching
 617 $\sim 5 \times 10^{-5}$ – $6 \times 10^{-5} \text{ s}^{-1}$ at noon. In contrast, the high-altitude TS site (1500 m a.s.l.)

618 shows lower values ($\sim 3 \times 10^{-5}$ – $4 \times 10^{-5} \text{ s}^{-1}$), consistent with its lower O_3 burden and
 619 cleaner background conditions. South China stations (GIG, SUST, GZ_ZL, GZ_NS,
 620 GZ_TM, GZ_GY, and GZ_DXC) display slightly higher peak $J(\text{O}(\text{D}))$ ($\sim 6 \times 10^{-5}$ –
 621 $7 \times 10^{-5} \text{ s}^{-1}$), in line with enhanced O_3 production under warm and humid subtropical
 622 conditions (Lu et al., 2025; Song et al., 2026; Zhang et al., 2025b). In Southwest
 623 China (CDAES and CQ), peak values ($\sim 5 \times 10^{-5}$ – $6 \times 10^{-5} \text{ s}^{-1}$) are comparable to those in
 624 South China, likely driven by basin topography that favors O_3 accumulation and
 625 vigorous photochemistry (Qiao et al., 2019; Shu et al., 2023; Wang et al., 2024a). The
 626 Central China site LY exhibits slightly lower peaks ($\sim 4 \times 10^{-5}$ – $5 \times 10^{-5} \text{ s}^{-1}$), similar to
 627 North and East China, indicating broadly comparable O_3 sources and photolysis
 628 efficiencies across these regions.

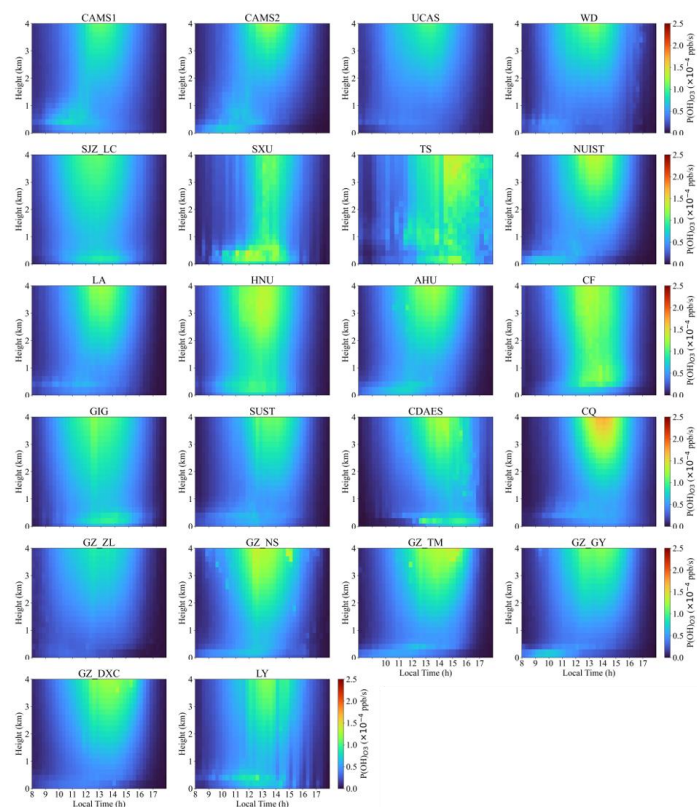


629

630 Figure 9. Mean diurnal vertical profiles of the O_3 photolysis rate, $J(\text{O}(\text{D}))$.

631 Figure 10 presents the mean diurnal vertical profiles of the OH production rate
 632 from ozone photolysis, $\text{P}(\text{OH})_{\text{O}_3}$, at the 22 sites, and seasonal mean diurnal
 633 variations are presented in Figures S29–S32. All sites exhibit a pronounced unimodal
 634 diurnal cycle, with $\text{P}(\text{OH})_{\text{O}_3}$ increasing rapidly after sunrise, peaking between 12:00

635 and 14:00 local time, and declining thereafter. The vertical location of the maxima
636 varies markedly among sites: at some, enhanced production is confined to the near-
637 surface layer (0–0.5 km), whereas at others distinct maxima occur at 3–4 km,
638 indicating substantial regional differences in photochemical regimes. Peak P(OH)₀₃
639 spans 0.5×10^{-4} – 2.0×10^{-4} ppb·s⁻¹ across the network. In North China (CAMS1,
640 CAMS2, UCAS, WD, SJZ_LC, and SXU), near-surface P(OH)₀₃ during 12:00–14:00
641 reaches 1.0×10^{-4} – 2.0×10^{-4} ppb·s⁻¹. The urban sites CAMS1, CAMS2, UCAS,
642 and WD show the highest values (1.5×10^{-4} – 2.0×10^{-4} ppb·s⁻¹), whereas SJZ_LC,
643 likely influenced by local emissions and complex topography, exhibits slightly lower
644 peaks (1.0×10^{-4} – 1.5×10^{-4} ppb·s⁻¹). SXU reaches $\sim 1.7 \times 10^{-4}$ ppb·s⁻¹. At all
645 these sites, P(OH)₀₃ decreases with altitude and generally falls below 1.0×10^{-4} ppb
646 ppb·s⁻¹ above 1 km. East China stations (TS, NUIST, LA, HNU, AHU, and CF)
647 display similar peak timing (12:00–14:00), with near-surface maxima of 1.0×10^{-4} –
648 1.8×10^{-4} ppb·s⁻¹. TS, NUIST, HNU, AHU, and CF reach $\sim 1.5 \times 10^{-4}$ – 1.8×10^{-4}
649 ppb·s⁻¹, while LA peaks at $\sim 1.4 \times 10^{-4}$ ppb·s⁻¹. In South China (GIG, SUST,
650 GZ_ZL, GZ_NS, GZ_TM, GZ_GY, and GZ_DXC), the maxima occur slightly later
651 (13:00–15:00) and are generally higher (1.3×10^{-4} – 1.7×10^{-4} ppb·s⁻¹), with
652 GZ_GY reaching $\sim 1.9 \times 10^{-4}$ ppb·s⁻¹ and GZ_NS, GZ_TM, and GZ_DXC
653 $\sim 1.8 \times 10^{-4}$ ppb·s⁻¹. Southwest China (CDAES and CQ) shows peaks of
654 $\sim 1.5 \times 10^{-4}$ – 2.5×10^{-4} ppb·s⁻¹, including $\sim 1.9 \times 10^{-4}$ ppb·s⁻¹ at CQ and
655 $\sim 1.5 \times 10^{-4}$ ppb·s⁻¹ at CDAES. The Central China site LY exhibits a peak of
656 $\sim 1.5 \times 10^{-4}$ ppb·s⁻¹, comparable to those in North and East China, indicating
657 broadly similar ozone photochemical efficiencies across these regions.



带格式的：居中

658

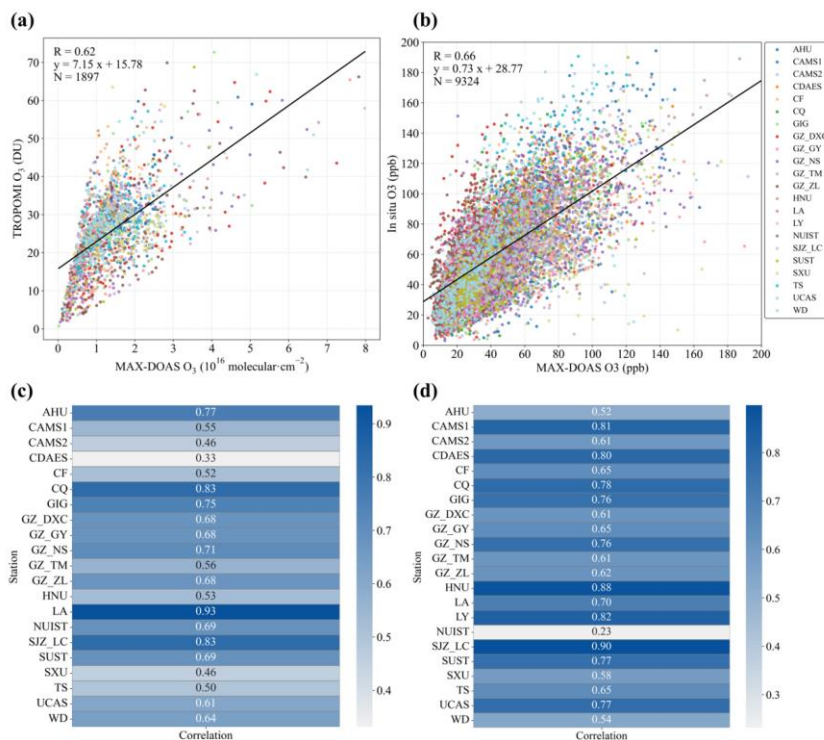
659 Figure 10. Mean vertical profiles of OH radicals produced by O₃ photolysis.

660

661 3.4 Validations with independent data

662 The dataset was validated using two independent approaches. First, O₃ VCD
 663 retrieved from the MAX-DOAS network for 2021–2024 were evaluated against
 664 coincident TROPOMI satellite observations. MAX-DOAS measurements were
 665 averaged within ± 30 min of the TROPOMI overpass (13:30–14:00 Beijing Time), and
 666 TROPOMI pixels were spatially averaged over a 7 km \times 5.5 km area center on each
 667 site, consistent with the native spatial resolution of TROPOMI. As shown in Figure
 668 11a, the two datasets exhibit a strong linear relationship, with a Pearson correlation
 669 coefficient of $R = 0.62$ ($N = 1897$); site-resolved correlations are given in Figure 11c.
 670 Second, near-surface O₃ concentrations retrieved at the 22 hyperspectral sites were
 671 compared with in situ measurements from the nearest CNEMC over the same period.
 672 Site pairs were selected following the spatial representativeness criteria of Song et al.
 673 (2023b), Specifically, we prioritized the nearest CNEMC station within a maximum
 674 distance of ~10–15 km (detailed in Table S1) and verified environmental consistency
 675 between the paired sites using land-use and satellite-derived products, ensuring that

676 both sites sampled comparable urban or suburban atmospheric conditions, and the
 677 separation distances are listed in Table S1; pairs that did not satisfy the matching
 678 requirements were excluded. The comparison (Figure 11b) shows a significant
 679 positive correlation ($R = 0.66$, $N = 9324$), demonstrating good consistency between
 680 MAX-DOAS-derived surface O_3 and ground-based observations. The correlations for
 681 each hyperspectral site and its nearest CNEMC are summarized in Figure 11d.
 682 Together, these two independent validations demonstrate reasonable consistency and
 683 provide confidence in the dataset used in this study.
 684 Together, these two independent validations confirm the reliability of the dataset used in this study.



685
 686 Figure 11. (a) Correlation between O_3 column densities retrieved from hyperspectral
 687 ground-based stations and TROPOMI satellite observations; (b) correlation between
 688 hyperspectral O_3 column densities and in situ O_3 measurements from the nearest
 689 CNEMC; (c) site-specific correlations between hyperspectral and TROPOMI O_3
 690 column densities; (d) site-specific correlations between hyperspectral O_3 column
 691 densities and in situ O_3 at the nearest CNEMC.

692
 693 **4. Data availability**

694 The vertical profiles of HONO and O_3 , and the vertical profiles of OH radicals
 695 over the major regions of China presented in this study, are freely available in .xlsx

696 format at Zenodo (<https://doi.org/10.5281/zenodo.18489836>; Zou et al., 2026).

697

698 5. Summary

699 We developed and released a comprehensive dataset of vertical profiles of
700 HONO and O₃, and the associated OH radical production rates, P(OH)_{HONO} and
701 P(OH)_{O₃}, derived from the Chinese hyperspectral vertical remote-sensing network for
702 2021–2024. The dataset spans 22 representative sites across North, East, Central,
703 South, and Southwest China, covering a wide range of climatic regimes and surface
704 types, and represents one of the most extensive [publicly available](#) collections in China
705 in terms of spatial coverage and vertical resolution of photochemical parameters
706 relevant to OH precursors. Independent validation against TROPOMI satellite
707 retrievals and in situ measurements from the CNEMC demonstrates robust
708 consistency. Mean diurnal profiles within 0–4 km reveal pronounced regional and
709 vertical contrasts in HONO and O₃ driven photochemistry. Both J(HONO) and
710 J(O(¹D)) exhibit radiation controlled, single-peaked diurnal cycles, with maxima
711 around local noon (11:00–14:00), and remain elevated in the upper mixed layer and
712 the lower free troposphere, reflecting the combined effects of radiative transfer and
713 aerosol extinction on the vertical distribution of photolysis rates. Accordingly,
714 P(OH)_{HONO} and P(OH)_{O₃} peak near the surface and decrease with height, indicating
715 that the boundary layer is the primary daytime source region of OH. At several
716 plateau and mountainous sites, however, the lower free troposphere also shows a
717 substantial radical production potential. Urban and highly industrialized sites exhibit
718 higher photolysis rates and OH production, reflecting the combined effects of high
719 precursor concentrations and strong radiation, while high-altitude clean-background
720 sites, despite lower near-surface concentrations, maintain relatively large photolysis
721 rates and significant OH production at middle and upper levels due to weaker aerosol
722 extinction and stronger shortwave radiation, showing a vertical photochemical
723 structure distinct from that over plains.

724 With continuous temporal coverage ranging from five months to 3.5 years and
725 multi-site vertical profiling, this dataset provides a valuable foundation for: (1)
726 quantifying the relative contributions of HONO and O₃ photolysis to the OH budget
727 in the boundary layer and the lower free troposphere; (2) constraining radical initial
728 conditions and radiative parameterizations in regional and global chemical transport
729 models; (3) enabling cross-validation and synergistic inversion among ground-based,
730 UAV, and satellite observations; (4) advancing studies of photochemical pollution
731 formation, secondary aerosol production, and atmospheric oxidation capacity; and (5)
732 supporting air-quality management and policy development as a complementary
733 national monitoring resource. [\(6\) serving as a critical benchmark for assessing and
734 reducing uncertainties in vertical parameterization schemes \(e.g., turbulent mixing,
735 photolysis rates, heterogeneous reactions\) within atmospheric chemical transport
736 models. However, it is important to note the limitations of the current dataset. The
737 time span \(2021–2024\) limits the capacity for robust analysis of long-term interannual](#)

设置了格式: 字体颜色: 文字 1

738 [trends driven by climate change or policy shifts. The observed photochemical regimes](#)
739 [may not fully represent conditions during extreme climatic years outside this period,](#)
740 [and the climatological representativeness of sites with shorter operational histories](#)
741 [requires continued data accumulation.](#)

设置了格式: 字体颜色: 文字 1

742

743 **Financial support**

744 This work was supported by the National Natural Science Foundation of China
745 (42588301, 42225504), the President's Foundation of Hefei Institutes of Physical
746 Science, Chinese Academy of Sciences (YZJJQY202401, BJPY2024B09).

747

748

749 **References**

750 Aliwell, S. R., Van Roozendaal, M., Johnston, P. V., Richter, A., Wagner, T.,
751 Arlander, D. W., Burrows, J. P., Fish, D. J., Jones, R. L., Tørnkvist, K. K.,
752 Lambert, J.-C., Pfeilsticker, K., and Pundt, I.: Analysis for BrO in zenith-sky
753 spectra: An intercomparison exercise for analysis improvement, *Journal of*
754 *Geophysical Research: Atmospheres*, 107, ACH 10-1-ACH 10-20,
755 <https://doi.org/10.1029/2001JD000329>, 2002.

带格式的: 缩进: 左侧: 0 厘米, 悬挂缩进: 2 字符,
首行缩进: -2 字符, 段落间距段后: 0.5 行

756 Ancellet, G., Viatte, C., Boynard, A., Ravetta, F., Pelon, J., Cailteau-Fischbach, C.,
757 Genau, P., Capo, J., Roy, A., and Nédélec, P.: Analysis of the day-to-day
758 variability of ozone vertical profiles in the lower troposphere during the 2022
759 Paris ACROSS campaign, *Atmospheric Chemistry and Physics*, 24, 12963–
760 12983, <https://doi.org/10.5194/acp-24-12963-2024>, 2024.

761 Andersen, S. T., Carpenter, L. J., Reed, C., Lee, J. D., Chance, R., Sherwen, T.,
762 Vaughan, A. R., Stewart, J., Edwards, P. M., Bloss, W. J., Sommariva, R.,
763 Crilley, L. R., Nott, G. J., Neves, L., Read, K., Heard, D. E., Seakins, P. W.,
764 Whalley, L. K., Boustead, G. A., Fleming, L. T., Stone, D., and Fomba, K. W.:
765 Extensive field evidence for the release of HONO from the photolysis of nitrate
766 aerosols, *Science Advances*, 9, eadd6266,
767 <https://doi.org/10.1126/sciadv.add6266>, 2023.

768 Anon: Systematic Evaluation of Four Satellite AOD Datasets for Estimating PM2.5
769 Using a Random Forest Approach, *Remote sensing*, 15, 2064–2064,
770 <https://doi.org/10.3390/rs15082064>, 2023.

771 Aumont, B., Chervier, F., and Laval, S.: Contribution of HONO sources to the
772 NO_x/HO_x/O₃ chemistry in the polluted boundary layer, *Atmospheric*
773 *Environment*, 37, 487–498, [https://doi.org/10.1016/S1352-2310\(02\)00920-2](https://doi.org/10.1016/S1352-2310(02)00920-2),
774 2003.

775 Chambers, S. D., Guérette, E.-A., Monk, K., Griffiths, A. D., Zhang, Y., Duc, H.,
776 Cope, M., Emmerson, K. M., Chang, L. T., Silver, J. D., Utembe, S., Crawford,
777 J., Williams, A. G., and Keywood, M.: Skill-Testing Chemical Transport Models

- 778 across Contrasting Atmospheric Mixing States Using Radon-222, *Atmosphere*,
779 10, 25, <https://doi.org/10.3390/atmos10010025>, 2019.
- 780 Chen, Z., Xie, Y., Liu, J., Shen, L., Cheng, X., Han, H., Yang, M., Shen, Y., Zhao, T.,
781 and Hu, J.: Distinct seasonality in vertical variations of tropospheric ozone over
782 coastal regions of southern China, *Science of The Total Environment*, 874,
783 162423, <https://doi.org/10.1016/j.scitotenv.2023.162423>, 2023.
- 784 Chen, Z., Liu, R., Wu, S., Xu, J., Wu, Y., and Qi, S.: Diurnal variation characteristics
785 and meteorological causes of autumn ozone in the Pearl River Delta, China,
786 *Science of The Total Environment*, 908, 168469,
787 <https://doi.org/10.1016/j.scitotenv.2023.168469>, 2024.
- 788 Couillard, M. H., Schwab, M. J., Schwab, J. J., Lu, C.-H. (Sarah), Joseph, E., Stutsrim,
789 B., Shrestha, B., Zhang, J., Knepp, T. N., and Gronoff, G. P.: Vertical Profiles of
790 Ozone Concentrations in the Lower Troposphere Downwind of New York City
791 During LISTOS 2018–2019, *Journal of Geophysical Research: Atmospheres*,
792 126, e2021JD035108, <https://doi.org/10.1029/2021JD035108>, 2021.
- 793 David, L. M. and Nair, P. R.: Diurnal and seasonal variability of surface ozone and
794 NO_x at a tropical coastal site: Association with mesoscale and synoptic
795 meteorological conditions, *Journal of Geophysical Research: Atmospheres*, 116,
796 <https://doi.org/10.1029/2010JD015076>, 2011.
- 797 Dewan, S. and Lakhani, A.: Tropospheric ozone and its natural precursors impacted
798 by climatic changes in emission and dynamics, *Front. Environ. Sci.*, 10,
799 <https://doi.org/10.3389/fenvs.2022.1007942>, 2022.
- 800 Donzelli, G. and Suarez-Varela, M. M.: Tropospheric Ozone: A Critical Review of
801 the Literature on Emissions, Exposure, and Health Effects, *Atmosphere*, 15, 779,
802 <https://doi.org/10.3390/atmos15070779>, 2024.
- 803 Elshorbany, Y., Barnes, I., Becker, K., Kleffmann, J., and Wiesen, P.: Sources and
804 cycling of tropospheric hydroxyl radicals - An overview, USF St. Petersburg
805 Campus Faculty Publications, 2010.
- 806 Fardilah, R. D., Turyanti, A., Pangestu, L. A., Dominica, M. V., and Perdinan:
807 Systematic Literature Review on Ozone Dispersion Correlated with Diurnal
808 Concentration Pattern in Urban and Rural Areas, *Agromet*, 37, 77–90,
809 <https://doi.org/10.29244/j.agromet.37.2.77-90>, 2023.
- 810 Fleischmann, O. C., Hartmann, M., Burrows, J. P., and Orphal, J.: New ultraviolet
811 absorption cross-sections of BrO at atmospheric temperatures measured by time-
812 windowing Fourier transform spectroscopy, *Journal of Photochemistry and*
813 *Photobiology A: Chemistry*, 168, 117–132,
814 <https://doi.org/10.1016/j.jphotochem.2004.03.026>, 2004.

- 815 Garcia-Nieto, D., Benavent, N., and Saiz-Lopez, A.: Measurements of atmospheric
816 HONO vertical distribution and temporal evolution in Madrid (Spain) using the
817 MAX-DOAS technique, *Science of The Total Environment*, 643, 957–966,
818 <https://doi.org/10.1016/j.scitotenv.2018.06.180>, 2018b.
- 819 Gu, R., Shen, H., Xue, L., Wang, T., Gao, J., Li, H., Liang, Y., Xia, M., Yu, C., Liu,
820 Y., and Wang, W.: Investigating the sources of atmospheric nitrous acid (HONO)
821 in the megacity of Beijing, China, *Science of The Total Environment*, 812,
822 152270, <https://doi.org/10.1016/j.scitotenv.2021.152270>, 2022.
- 823 Guo, J., Zhang, X., Gao, Y., Wang, Z., Zhang, M., Xue, W., Herrmann, H., Brasseur,
824 G. P., Wang, T., and Wang, Z.: Evolution of Ozone Pollution in China: What
825 Track Will It Follow?, *Environ. Sci. Technol.*, 57, 109–117,
826 <https://doi.org/10.1021/acs.est.2c08205>, 2023.
- 827 Guo, P., Su, Y., Sun, X., Liu, C., Cui, B., Xu, X., Ouyang, Z., and Wang, X.: Urban–
828 Rural Comparisons of Biogenic Volatile Organic Compounds and Ground-Level
829 Ozone in Beijing, *Forests*, 15, 508, <https://doi.org/10.3390/f15030508>, 2024a.
- 830 Guo, W., Yang, Y., Zhang, J., Han, K., Yang, Y., Chen, Q., Li, S., and Zhu, Y.:
831 Effects of valley topography on ozone pollution in the Lanzhou valley: A
832 numerical case study, *Environ Pollut*, 363, 125225,
833 <https://doi.org/10.1016/j.envpol.2024.125225>, 2024b.
- 834 Hao, Q., Jiang, N., Zhang, R., Yang, L., and Li, S.: Characteristics, sources, and
835 reactions of nitrous acid during winter at an urban site in the Central Plains
836 Economic Region in China, *Atmospheric Chemistry and Physics*, 20, 7087–7102,
837 <https://doi.org/10.5194/acp-20-7087-2020>, 2020.
- 838 He, C., Wu, Q., Li, B., Liu, J., Gong, X., and Zhang, L.: Surface ozone pollution in
839 China: Trends, exposure risks, and drivers, *Front. Public Health*, 11,
840 <https://doi.org/10.3389/fpubh.2023.1131753>, 2023a.
- 841 He, G., He, C., Wang, H., Lu, X., Pei, C., Qiu, X., Liu, C., Wang, Y., Liu, N., Zhang,
842 J., Lei, L., Liu, Y., Wang, H., Deng, T., Fan, Q., and Fan, S.: Nighttime ozone in
843 the lower boundary layer: insights from 3-year tower-based measurements in
844 South China and regional air quality modeling, *Atmospheric Chemistry and
845 Physics*, 23, 13107–13124, <https://doi.org/10.5194/acp-23-13107-2023>, 2023b.
- 846 He, S., Wang, S., Zhang, S., Zhu, J., Sun, Z., Xue, R., and Zhou, B.: Vertical
847 distributions of atmospheric HONO and the corresponding OH radical
848 production by photolysis at the suburb area of Shanghai, China, *Science of The
849 Total Environment*, 858, 159703,
850 <https://doi.org/10.1016/j.scitotenv.2022.159703>, 2023c.
- 851 He, Y., Wang, H., Wang, H., Xu, X., Li, Y., and Fan, S.: Meteorology and
852 topographic influences on nocturnal ozone increase during the summertime over

- 853 Shaoguan, China, *Atmospheric Environment*, 256, 118459,
854 <https://doi.org/10.1016/j.atmosenv.2021.118459>, 2021.
- 855 Hu, Q., Ji, X., Hong, Q., Li, J., Li, Q., Ou, J., Liu, H., Xing, C., Tan, W., Chen, J.,
856 Chang, B., and Liu, C.: Vertical Evolution of Ozone Formation Sensitivity Based
857 on Synchronous Vertical Observations of Ozone and Proxies for Its Precursors:
858 Implications for Ozone Pollution Prevention Strategies, *Environ Sci Technol*, 58,
859 4291–4301, <https://doi.org/10.1021/acs.est.4c00637>, 2024.
- 860 Itahashi, S., Mathur, R., Hogrefe, C., and Zhang, Y.: Modeling stratospheric intrusion
861 and trans-Pacific transport on tropospheric ozone using hemispheric CMAQ
862 during April 2010 – Part 1: Model evaluation and air mass characterization for
863 stratosphere–troposphere transport, *Atmospheric Chemistry and Physics*, 20,
864 3373–3396, <https://doi.org/10.5194/acp-20-3373-2020>, 2020.
- 865 Ji, X., Liu, C., Wang, Y., Hu, Q., Lin, H., Zhao, F., Xing, C., Tang, G., Zhang, J., and
866 Wagner, T.: Ozone profiles without blind area retrieved from MAX-DOAS
867 measurements and comprehensive validation with multi-platform observations,
868 *Remote Sensing of Environment*, 284, 113339,
869 <https://doi.org/10.1016/j.rse.2022.113339>, 2023.
- 870 Johnson, M. S., Rozanov, A., Weber, M., Mettig, N., Sullivan, J., Newchurch, M. J.,
871 Kuang, S., Leblanc, T., Chouza, F., Berkoff, T. A., Gronoff, G., Strawbridge, K.
872 B., Alvarez, R. J., Langford, A. O., Senff, C. J., Kirgis, G., McCarty, B., and
873 Twigg, L.: TOLNet validation of satellite ozone profiles in the troposphere:
874 impact of retrieval wavelengths, *Atmospheric Measurement Techniques*, 17,
875 2559–2582, <https://doi.org/10.5194/amt-17-2559-2024>, 2024.
- 876 Kim, H., Park, R. J., Hong, S.-Y., Park, D.-H., Kim, S.-W., Oak, Y. J., Feng, X., Lin,
877 H., and Fu, T.-M.: A mixed layer height parameterization in a 3-D chemical
878 transport model: Implications for gas and aerosol simulations, *Sci Total Environ*,
879 955, 176838, <https://doi.org/10.1016/j.scitotenv.2024.176838>, 2024.
- 880 Li, K., Jacob, D. J., Shen, L., Lu, X., De Smedt, I., and Liao, H.: Increases in surface
881 ozone pollution in China from 2013 to 2019: anthropogenic and meteorological
882 influences, *Atmospheric Chemistry and Physics*, 20, 11423–11433,
883 <https://doi.org/10.5194/acp-20-11423-2020>, 2020.
- 884 Li, K., Tan, R., Qiao, W., Lee, T., Wang, Y., Zhang, D., Tang, M., Zhao, W., Gu, Y.,
885 Fan, S., Zhang, J., Lyu, X., Xue, L., Xu, J., Ma, Z., Latif, M. T., Amnuaylojaroen,
886 T., Gil, J., Lee, M.-H., Bak, J., Kim, J., Liao, H., Kanaya, Y., Lu, X., Nagashima,
887 T., and Koo, J.-H.: Surface and tropospheric ozone over East Asia and Southeast
888 Asia from observations: distributions, trends, and variability, *Atmospheric
889 Chemistry and Physics*, 25, 11575–11596, [https://doi.org/10.5194/acp-25-11575-
890 2025](https://doi.org/10.5194/acp-25-11575-2025), 2025a.

- 891 Li, M., McDonald, B. C., McKeen, S. A., Eskes, H., Levelt, P., Francoeur, C.,
892 Harkins, C., He, J., Barth, M., Henze, D. K., Bela, M. M., Trainer, M., de Gouw,
893 J. A., and Frost, G. J.: Assessment of Updated Fuel-Based Emissions Inventories
894 Over the Contiguous United States Using TROPOMI NO₂ Retrievals, *Journal of*
895 *Geophysical Research: Atmospheres*, 126, e2021JD035484,
896 <https://doi.org/10.1029/2021JD035484>, 2021.
- 897 Li, Y., Xing, C., Peng, H., Jiao, P., Zhang, Q., Liu, C., Sun, Z., Tan, W., and Liu, C.:
898 Vertical Differences in NO₂-to-HONO Heterogeneous Conversion and HONO-
899 Driven OH Production over Inland, Coastal, and Island Regions, *Environ. Sci.*
900 *Technol.*, 59, 26020–26030, <https://doi.org/10.1021/acs.est.5c10318>, 2025b.
- 901 Liang, Y., Zha, Q., Wang, W., Cui, L., Lui, K. H., Ho, K. F., Wang, Z., Lee, S., and
902 Wang, T.: Revisiting nitrous acid (HONO) emission from on-road vehicles: A
903 tunnel study with a mixed fleet, *Journal of the Air & Waste Management*
904 *Association*, 67, 797–805, <https://doi.org/10.1080/10962247.2017.1293573>,
905 2017.
- 906 Liao, Z., Pan, Y., Ma, P., Jia, X., Cheng, Z., Wang, Q., Dou, Y., Zhao, X., Zhang, J.,
907 and Quan, J.: Meteorological and chemical controls on surface ozone diurnal
908 variability in Beijing: A clustering-based perspective, *Atmospheric Environment*,
909 295, 119566, <https://doi.org/10.1016/j.atmosenv.2022.119566>, 2023.
- 910 Liao, Z., Gao, M., Zhang, J., Sun, J., Quan, J., Jia, X., Pan, Y., and Fan, S.: Mixing-
911 layer-height-referenced ozone vertical distribution in the lower troposphere of
912 Chinese megacities: stratification, classification, and meteorological and
913 photochemical mechanisms, *Atmospheric Chemistry and Physics*, 24, 3541–
914 3557, <https://doi.org/10.5194/acp-24-3541-2024>, 2024.
- 915 Liao, Z., Zhang, J., Gao, M., and Ma, Z.: Widespread stratospheric intrusion influence
916 on summer ozone pollution over China revealed by multi-site ozonesonde and
917 validated EAC4 reanalysis, *Atmospheric Chemistry and Physics*, 25, 14865–
918 14877, <https://doi.org/10.5194/acp-25-14865-2025>, 2025.
- 919 Lin, H., Xing, C., Hong, Q., Liu, C., Ji, X., Liu, T., Lin, J., Lu, C., Tan, W., Li, Q.,
920 and Liu, H.: Diagnosis of Ozone Formation Sensitivities in Different Height
921 Layers via MAX-DOAS Observations in Guangzhou, *Journal of Geophysical*
922 *Research: Atmospheres*, 127, e2022JD036803,
923 <https://doi.org/10.1029/2022JD036803>, 2022.
- 924 Liu, C., Xing, C., Hu, Q., Li, Q., Liu, H., Hong, Q., Tan, W., Ji, X., Lin, H., Lu, C.,
925 Lin, J., Liu, H., Wei, S., Chen, J., Yang, K., Wang, S., Liu, T., and Chen, Y.:
926 Ground-Based Hyperspectral Stereoscopic Remote Sensing Network: A
927 Promising Strategy to Learn Coordinated Control of O₃ and PM_{2.5} over China,
928 *Engineering*, 19, 71–83, <https://doi.org/10.1016/j.eng.2021.02.019>, 2022a.

- 929 Liu, H., Han, X., Tang, G., Zhang, J., Xia, X., Zhang, M., and Meng, L.: Model
930 analysis of vertical exchange of boundary layer ozone and its impact on surface
931 air quality over the North China Plain, *Science of The Total Environment*, 821,
932 153436, <https://doi.org/10.1016/j.scitotenv.2022.153436>, 2022b.
- 933 Liu, P., Xue, C., Ye, C., Liu, C., Zhang, C., Wang, J., Zhang, Y., Liu, J., and Mu, Y.:
934 The Lack of HONO Measurement May Affect the Accurate Diagnosis of Ozone
935 Production Sensitivity, *ACS Environ. Au*, 3, 18–23,
936 <https://doi.org/10.1021/acsenvironau.2c00048>, 2023a.
- 937 Liu, X., Yi, G., Zhou, X., Zhang, T., Bie, X., Li, J., and Tan, H.: Spatio-temporal
938 variations of PM_{2.5} and O₃ in China during 2013–2021: Impact factor analysis,
939 *Environmental Pollution*, 334, 122189,
940 <https://doi.org/10.1016/j.envpol.2023.122189>, 2023b.
- 941 Lu, Y., Kong, L., Shen, J., Liu, B., An, Y., Wang, Y., Tan, J., and Wang, L.:
942 Characteristics and influencing factors of ambient ozone pollution in Hangzhou
943 in the relative humidity range with high ozone levels, *Atmospheric Pollution
944 Research*, 16, 102648, <https://doi.org/10.1016/j.apr.2025.102648>, 2025.
- 945 Lyu, Y., Xu, H., Wu, H., Han, F., Lv, F., Kang, A., and Pang, X.: Spatiotemporal
946 variations of PM_{2.5} and ozone in urban agglomerations of China and
947 meteorological drivers for ozone using explainable machine learning,
948 *Environmental Pollution*, 365, 125380,
949 <https://doi.org/10.1016/j.envpol.2024.125380>, 2025.
- 950 Meng, F., Qin, M., Tang, K., Duan, J., Fang, W., Liang, S., Ye, K., Xie, P., Sun, Y.,
951 Xie, C., Ye, C., Fu, P., Liu, J., and Liu, W.: High-resolution vertical distribution
952 and sources of HONO and NO₂ in the nocturnal boundary layer in urban Beijing,
953 China, *Atmospheric Chemistry and Physics*, 20, 5071–5092,
954 <https://doi.org/10.5194/acp-20-5071-2020>, 2020.
- 955 Monks, P. S., Archibald, A. T., Colette, A., Cooper, O., Coyle, M., Derwent, R.,
956 Fowler, D., Granier, C., Law, K. S., Mills, G. E., Stevenson, D. S., Tarasova, O.,
957 Thouret, V., von Schneidmesser, E., Sommariva, R., Wild, O., and Williams, M.
958 L.: Tropospheric ozone and its precursors from the urban to the global scale from
959 air quality to short-lived climate forcer, *Atmospheric Chemistry and Physics*, 15,
960 8889–8973, <https://doi.org/10.5194/acp-15-8889-2015>, 2015.
- 961 Orphal, J. and Chance, K.: Ultraviolet and visible absorption cross-sections for
962 HITRAN, *Journal of Quantitative Spectroscopy and Radiative Transfer*, 82, 491–
963 504, [https://doi.org/10.1016/S0022-4073\(03\)00173-0](https://doi.org/10.1016/S0022-4073(03)00173-0), 2003.
- 964 Park, S., Son, S.-W., Jung, M.-I., Park, J., and Park, S. S.: Evaluation of tropospheric
965 ozone reanalyses with independent ozonesonde observations in East Asia, *Geosci.
966 Lett.*, 7, 12, <https://doi.org/10.1186/s40562-020-00161-9>, 2020.

- 967 Qiao, X., Guo, H., Wang, P., Tang, Y., Ying, Q., Zhao, X., Deng, W., and Zhang, H.:
968 Fine Particulate Matter and Ozone Pollution in the 18 Cities of the Sichuan Basin
969 in Southwestern China: Model Performance and Characteristics, *Aerosol Air*
970 *Qual. Res.*, 19, 2308–2319, <https://doi.org/10.4209/aaqr.2019.05.0235>, 2019.
- 971 Qiu, Y., Li, X., Chai, W., Liu, Y., Song, M., Tian, X., Zou, Q., Lou, W., Zhang, W.,
972 Li, J., and Zhang, Y.: Insights into ozone pollution control in urban areas by
973 decoupling meteorological factors based on machine learning, *Atmospheric*
974 *Chemistry and Physics*, 25, 1749–1763, [https://doi.org/10.5194/acp-25-1749-](https://doi.org/10.5194/acp-25-1749-2025)
975 [2025](https://doi.org/10.5194/acp-25-1749-2025), 2025.
- 976 Qu, H., Wang, Y., Zhang, R., and Li, J.: Extending Ozone-Precursor Relationships in
977 China From Peak Concentration to Peak Time, *Journal of Geophysical Research:*
978 *Atmospheres*, 125, e2020JD033670, <https://doi.org/10.1029/2020JD033670>,
979 2020.
- 980 R. Crilley, L., Kramer, L., D. Pope, F., K. Whalley, L., R. Cryer, D., E. Heard, D.,
981 D. Lee, J., Reed, C., and J. Bloss, W.: On the interpretation of in situ HONO
982 observations via photochemical steady state, *Faraday Discussions*, 189, 191–212,
983 <https://doi.org/10.1039/C5FD00224A>, 2016.
- 984 Ryan, R. G., Rhodes, S., Tully, M., Wilson, S., Jones, N., Frieß, U., and Schofield, R.:
985 Daytime HONO, NO₂ and aerosol distributions from MAX-DOAS observations
986 in Melbourne, *Atmospheric Chemistry and Physics*, 18, 13969–13985,
987 <https://doi.org/10.5194/acp-18-13969-2018>, 2018a.
- 988 Sekiya, T., Emili, E., Miyazaki, K., Inness, A., Qu, Z., Pierce, R. B., Jones, D.,
989 Worden, H., Cheng, W. Y. Y., Huijnen, V., and Koren, G.: Assessing the relative
990 impacts of satellite ozone and its precursor observations to improve global
991 tropospheric ozone analysis using multiple chemical reanalysis systems,
992 *Atmospheric Chemistry and Physics*, 25, 2243–2268,
993 <https://doi.org/10.5194/acp-25-2243-2025>, 2025.
- 994 Serdyuchenko, A., Gorshchev, V., Weber, M., Chehade, W., and Burrows, J. P.: High
995 spectral resolution ozone absorption cross-sections – Part 2: Temperature
996 dependence, *Atmospheric Measurement Techniques*, 7, 625–636,
997 <https://doi.org/10.5194/amt-7-625-2014>, 2014.
- 998 Sharma, B. R., Kuttippurath, J., and Gopikrishnan, G. S.: Tropospheric ozone as an
999 atmospheric pollutant and short-lived climate forcer in the Third Pole,
1000 *Chemosphere*, 380, 144474, <https://doi.org/10.1016/j.chemosphere.2025.144474>,
1001 2025.
- 1002 Shi, Y., Zeng, Q., Liu, L., Huo, J., Zhang, Z., Ding, W., and Hu, F.: Observed
1003 Evidence That Subsidence Process Stabilizes the Boundary Layer and Increases
1004 the Ground Concentration of Secondary Pollutants, *Journal of Geophysical*

- 1005 Research: Atmospheres, 127, e2021JD035244,
1006 <https://doi.org/10.1029/2021JD035244>, 2022.
- 1007 Shu, Z., Zhao, T., Chen, Y., Liu, Y., Yang, F., Jiang, Y., He, G., Yang, Q., and Zhang,
1008 Y.: Terrain effect on atmospheric process in seasonal ozone variation over the
1009 Sichuan Basin, Southwest China, *Environmental Pollution*, 338, 122622,
1010 <https://doi.org/10.1016/j.envpol.2023.122622>, 2023.
- 1011 Song, M., Zhao, X., Liu, P., Mu, J., He, G., Zhang, C., Tong, S., Xue, C., Zhao, X.,
1012 Ge, M., and Mu, Y.: Atmospheric NO_x oxidation as major sources for nitrous
1013 acid (HONO), *npj Clim Atmos Sci*, 6, 30, <https://doi.org/10.1038/s41612-023-00357-8>, 2023a.
- 1015 Song, X., Li, X.-B., Yuan, B., He, X., Chen, Y., Wang, S., Huangfu, Y., Peng, Y.,
1016 Zhang, C., Liu, A., Yang, H., Liu, C., Li, J., and Shao, M.: Elucidating key
1017 factors in regulating budgets of ozone and its precursors in atmospheric
1018 boundary layer, *npj Clim Atmos Sci*, 7, 262, <https://doi.org/10.1038/s41612-024-00818-8>, 2024.
- 1020 Song, Y., Xing, C., Liu, C., Lin, J., Wu, H., Liu, T., Lin, H., Zhang, C., Tan, W., Ji,
1021 X., Liu, H., and Li, Q.: Evaluation of transport processes over North China Plain
1022 and Yangtze River Delta using MAX-DOAS observations, *Atmospheric
1023 Chemistry and Physics*, 23, 1803–1824, <https://doi.org/10.5194/acp-23-1803-2023>, 2023b.
- 1025 Song, Y., Wang, P., Yang, Y., Tang, J., and Liao, H.: Meteorological conditions and
1026 physicochemical processes amplifying ozone pollution during heatwaves in
1027 major city clusters of China, *Atmospheric Research*, 330, 108580,
1028 <https://doi.org/10.1016/j.atmosres.2025.108580>, 2026.
- 1029 Spataro, F. and Ianniello, A.: Sources of atmospheric nitrous acid: State of the science,
1030 current research needs, and future prospects, *Journal of the Air & Waste
1031 Management Association*, 64, 1232–1250,
1032 <https://doi.org/10.1080/10962247.2014.952846>, 2014.
- 1033 Spurr, R. J. D.: VLIDORT: A linearized pseudo-spherical vector discrete ordinate
1034 radiative transfer code for forward model and retrieval studies in multilayer
1035 multiple scattering media, *Journal of Quantitative Spectroscopy and Radiative
1036 Transfer*, 102, 316–342, <https://doi.org/10.1016/j.jqsrt.2006.05.005>, 2006.
- 1037 Stutz, J., Kim, E. S., Platt, U., Bruno, P., Perrino, C., and Febo, A.: UV-visible
1038 absorption cross sections of nitrous acid, *Journal of Geophysical Research:
1039 Atmospheres*, 105, 14585–14592, <https://doi.org/10.1029/2000JD900003>, 2000.
- 1040 Su, W., Liu, C., Hu, Q., Fan, G., Xie, Z., Huang, X., Zhang, T., Chen, Z., Dong, Y., Ji,
1041 X., Liu, H., Wang, Z., and Liu, J.: Characterization of ozone in the lower
1042 troposphere during the 2016 G20 conference in Hangzhou, *Sci Rep*, 7, 17368,

- 1043 <https://doi.org/10.1038/s41598-017-17646-x>, 2017.
- 1044 Tang, Y., An, J., Wang, F., Li, Y., Qu, Y., Chen, Y., and Lin, J.: Impacts of an
1045 unknown daytime HONO source on the mixing ratio and budget of HONO, and
1046 hydroxyl, hydroperoxyl, and organic peroxy radicals, in the coastal regions of
1047 China, *Atmospheric Chemistry and Physics*, 15, 9381–9398,
1048 <https://doi.org/10.5194/acp-15-9381-2015>, 2015.
- 1049 Thalman, R. and Volkamer, R.: Temperature dependent absorption cross-sections of
1050 O₂–O₂ collision pairs between 340 and 630 nm and at atmospherically relevant
1051 pressure, *Phys. Chem. Chem. Phys.*, 15, 15371,
1052 <https://doi.org/10.1039/c3cp50968k>, 2013.
- 1053 Thürkow, M., Schaap, M., Kranenburg, R., Pfäfflin, F., Neunhäuserer, L., Wolke, R.,
1054 Heinold, B., Stoll, J., Lupaşcu, A., Nordmann, S., Minkos, A., and Butler, T.:
1055 Dynamic evaluation of modeled ozone concentrations in Germany with four
1056 chemistry transport models, *Science of The Total Environment*, 906, 167665,
1057 <https://doi.org/10.1016/j.scitotenv.2023.167665>, 2024.
- 1058 Torres, O., Jethva, H., Ahn, C., Jaross, G., and Loyola, D. G.: TROPOMI aerosol
1059 products: evaluation and observations of synoptic-scale carbonaceous aerosol
1060 plumes during 2018–2020, *Atmospheric Measurement Techniques*, 13, 6789–
1061 6806, <https://doi.org/10.5194/amt-13-6789-2020>, 2020b.
- 1062 Vandaele, A. C., Hermans, C., Simon, P. C., Carleer, M., Colin, R., Fally, S.,
1063 Mérienne, M. F., Jenouvrier, A., and Coquart, B.: Measurements of the NO₂
1064 absorption cross-section from 42 000 cm⁻¹ to 10 000 cm⁻¹ (238–1000 nm) at
1065 220 K and 294 K, *Journal of Quantitative Spectroscopy and Radiative Transfer*,
1066 59, 171–184, [https://doi.org/10.1016/S0022-4073\(97\)00168-4](https://doi.org/10.1016/S0022-4073(97)00168-4), 1998.
- 1067 Wang, N., Du, Y., Chen, D., Meng, H., Chen, X., Zhou, L., Shi, G., Zhan, Y., Feng,
1068 M., Li, W., Chen, M., Li, Z., and Yang, F.: Spatial disparities of ozone pollution
1069 in the Sichuan Basin spurred by extreme, hot weather, *Atmospheric Chemistry
1070 and Physics*, 24, 3029–3042, <https://doi.org/10.5194/acp-24-3029-2024>, 2024a.
- 1071 Wang, R., Shen, H., Zeng, C., Chen, J., Wang, Y., and Li, Y.: A global land daily 10-
1072 km-resolution surface ozone dataset from 2013–2022, *Sci Data*, 12, 1710,
1073 <https://doi.org/10.1038/s41597-025-05990-x>, 2025a.
- 1074 Wang, W.-N., Cheng, T.-H., Gu, X.-F., Chen, H., Guo, H., Wang, Y., Bao, F.-W., Shi,
1075 S.-Y., Xu, B.-R., Zuo, X., Meng, C., and Zhang, X.-C.: Assessing Spatial and
1076 Temporal Patterns of Observed Ground-level Ozone in China, *Sci Rep*, 7, 3651,
1077 <https://doi.org/10.1038/s41598-017-03929-w>, 2017.
- 1078 Wang, X., Zhang, H., Hong, X., Xiang, Y., Wang, S., Zhang, T., Qin, Z., and Ou, J.:
1079 Vertical profiles and regional transport of ozone in typical area of Yangtze-
1080 Huaihe River Basin during the autumn base on multiple lidars, *Atmospheric*

- 1081 Pollution Research, 15, 101983, <https://doi.org/10.1016/j.apr.2023.101983>,
1082 2024b.
- 1083 Wang, Y., Puķite, J., Wagner, T., Donner, S., Beirle, S., Hilboll, A., Vrekoussis, M.,
1084 Richter, A., Apituley, A., PETERS, A., Allaart, M., Eskes, H., Frumau, A., Van
1085 Roozendaal, M., Lampel, J., Platt, U., Schmitt, S., Swart, D., and Vonk, J.:
1086 Vertical Profiles of Tropospheric Ozone From MAX-DOAS Measurements
1087 During the CINDI-2 Campaign: Part 1—Development of a New Retrieval
1088 Algorithm, *Journal of Geophysical Research: Atmospheres*, 123, 10,637-10,670,
1089 <https://doi.org/10.1029/2018JD028647>, 2018.
- 1090 Wang, Y., Dörner, S., Donner, S., Böhne, S., De Smedt, I., Dickerson, R. R., Dong,
1091 Z., He, H., Li, Z., Li, Z., Li, D., Liu, D., Ren, X., Theys, N., Wang, Y., Wang, Y.,
1092 Wang, Z., Xu, H., Xu, J., and Wagner, T.: Vertical profiles of NO₂, SO₂, HONO,
1093 HCHO, CHOCHO and aerosols derived from MAX-DOAS measurements at a
1094 rural site in the central western North China Plain and their relation to emission
1095 sources and effects of regional transport, *Atmospheric Chemistry and Physics*, 19,
1096 5417–5449, <https://doi.org/10.5194/acp-19-5417-2019>, 2019.
- 1097 Wang, Y., Gao, W., Wang, S., Song, T., Gong, Z., Ji, D., Wang, L., Liu, Z., Tang, G.,
1098 Huo, Y., Tian, S., Li, J., Li, M., Yang, Y., Chu, B., Petäjä, T., Kerminen, V.-M.,
1099 He, H., Hao, J., Kulmala, M., Wang, Y., and Zhang, Y.: Contrasting trends of
1100 PM_{2.5} and surface-ozone concentrations in China from 2013 to 2017, *Natl Sci*
1101 *Rev*, 7, 1331–1339, <https://doi.org/10.1093/nsr/nwaa032>, 2020.
- 1102 Wang, Y., Yang, Y., Yuan, Q., Li, T., Zhou, Y., Zong, L., Wang, M., Xie, Z., Ho, H.
1103 C., Gao, M., Tong, S., Lolli, S., and Zhang, L.: Substantially underestimated
1104 global health risks of current ozone pollution, *Nat Commun*, 16, 102,
1105 <https://doi.org/10.1038/s41467-024-55450-0>, 2025b.
- 1106 Wang, Z., Zhang, H., Shi, C., Ji, X., Zhu, Y., Xia, C., Sun, X., Zhang, M., Lin, X.,
1107 Yan, S., Zhou, Y., Xing, C., Chen, Y., and Liu, C.: Vertical and spatial
1108 differences in ozone formation sensitivities under different ozone pollution levels
1109 in eastern Chinese cities, *npj Clim Atmos Sci*, 8, 30,
1110 <https://doi.org/10.1038/s41612-024-00855-3>, 2025c.
- 1111 Xia, N., Du, E., Guo, Z., and de Vries, W.: The diurnal cycle of summer tropospheric
1112 ozone concentrations across Chinese cities: Spatial patterns and main drivers,
1113 *Environmental Pollution*, 286, 117547,
1114 <https://doi.org/10.1016/j.envpol.2021.117547>, 2021.
- 1115 Xing, C., Liu, C., Wang, S., Chan, K. L., Gao, Y., Huang, X., Su, W., Zhang, C.,
1116 Dong, Y., Fan, G., Zhang, T., Chen, Z., Hu, Q., Su, H., Xie, Z., and Liu, J.:
1117 Observations of the vertical distributions of summertime atmospheric pollutants
1118 and the corresponding ozone production in Shanghai, China, *Atmospheric*
1119 *Chemistry and Physics*, 17, 14275–14289, <https://doi.org/10.5194/acp-17-14275->

1120 2017, 2017.

1121 Xing, C., Liu, C., Wang, S., Hu, Q., Liu, H., Tan, W., Zhang, W., Li, B., and Liu, J.:
1122 A new method to determine the aerosol optical properties from multiple-
1123 wavelength O₄ absorptions by MAX-DOAS observation, *Atmospheric*
1124 *Measurement Techniques*, 12, 3289–3302, [https://doi.org/10.5194/amt-12-3289-](https://doi.org/10.5194/amt-12-3289-2019)
1125 2019, 2019.

1126 Xing, C., Liu, C., Wu, H., Lin, J., Wang, F., Wang, S., and Gao, M.: Ground-based
1127 vertical profile observations of atmospheric composition on the Tibetan Plateau
1128 (2017–2019), *Earth System Science Data*, 13, 4897–4912,
1129 <https://doi.org/10.5194/essd-13-4897-2021>, 2021a.

1130 Xing, C., Liu, C., Hu, Q., Fu, Q., Wang, S., Lin, H., Zhu, Y., Wang, S., Wang, W.,
1131 Javed, Z., Ji, X., and Liu, J.: Vertical distributions of wintertime atmospheric
1132 nitrogenous compounds and the corresponding OH radicals production in Leshan,
1133 southwest China, *Journal of Environmental Sciences*, 105, 44–55,
1134 <https://doi.org/10.1016/j.jes.2020.11.019>, 2021b.

1135 Xing, C., Liu, C., Hong, Q., Liu, H., Wu, H., Lin, J., Song, Y., Chen, Y., Liu, T., Hu,
1136 Q., Tan, W., and Lin, H.: Vertical distributions and potential sources of
1137 wintertime atmospheric pollutants and the corresponding ozone production on
1138 the coast of Bohai Sea, *Journal of Environmental Management*, 319, 115721,
1139 <https://doi.org/10.1016/j.jenvman.2022.115721>, 2022.

1140 Xing, C., Xu, S., Song, Y., Liu, C., Liu, Y., Lu, K., Tan, W., Zhang, C., Hu, Q., Wang,
1141 S., Wu, H., and Lin, H.: A new insight into the vertical differences in NO₂
1142 heterogeneous reaction to produce HONO over inland and marginal seas,
1143 *Atmospheric Chemistry and Physics*, 23, 5815–5834,
1144 <https://doi.org/10.5194/acp-23-5815-2023>, 2023.

1145 Xing, C., Liu, C., Li, Q., Wang, S., Tan, W., Zou, T., Wang, Z., and Lu, C.:
1146 Observations of HONO and its precursors between urban and its surrounding
1147 agricultural fields: The vertical transports, sources and contribution to OH,
1148 *Science of The Total Environment*, 915, 169159,
1149 <https://doi.org/10.1016/j.scitotenv.2023.169159>, 2024a.

1150 Xing, C., Liu, C., Ye, C., Xue, J., Wu, H., Ji, X., Ou, J., and Hu, Q.: Observations of
1151 the vertical distributions of summertime atmospheric pollutants in Nam Co: OH
1152 production and source analysis, *Atmospheric Chemistry and Physics*, 24, 10093–
1153 10112, <https://doi.org/10.5194/acp-24-10093-2024>, 2024c.

1154 Xu, S., Wang, S., Xia, M., Lin, H., Xing, C., Ji, X., Su, W., Tan, W., Liu, C., and Hu,
1155 Q.: Observations by Ground-Based MAX-DOAS of the Vertical Characters of
1156 Winter Pollution and the Influencing Factors of HONO Generation in Shanghai,
1157 China, *Remote Sensing*, 13, 3518, <https://doi.org/10.3390/rs13173518>, 2021.

- 1158 Xuan, H., Liu, J., Zhao, Y., Cao, Q., Chen, T., Wang, Y., Liu, Z., Sun, X., Li, H.,
1159 Zhang, P., Chu, B., Ma, Q., and He, H.: Relative humidity driven nocturnal
1160 HONO formation mechanism in autumn haze events of Beijing, *npj Clim Atmos*
1161 *Sci*, 7, 193, <https://doi.org/10.1038/s41612-024-00745-8>, 2024.
- 1162 Xuan, H., Lian, C., Ma, P., Lan, L., Wang, W., Liu, C., Quan, J., Zhang, S., Liu, J., Li,
1163 H., Chen, T., Zhang, P., Wang, Y., Chu, B., Ma, Q., and He, H.: Vertical
1164 Distribution of Sources and Atmospheric Impacts of HONO in the North China
1165 Plain, *Environ. Sci. Technol.*, 59, 17666–17676,
1166 <https://doi.org/10.1021/acs.est.5c01801>, 2025b.
- 1167 Xue, C., Ye, C., Zhang, C., Catoire, V., and Mu, Y.: Evidence for Strong HONO
1168 Emission from Fertilized Agricultural Fields and its Remarkable Impact on
1169 Regional O₃ Pollution in the Summer North China Plain, *ACS Earth and Space*
1170 *Chemistry*, 5, <https://doi.org/10.1021/acsearthspacechem.0c00314>, 2021.
- 1171 Xue, C., Chen, H., McGillen, M. R., Su, H., Cheng, Y., Kleffmann, J., Li, G.,
1172 Cazaunau, M., Colomb, A., Sciare, J., DeWitt, L., Marchand, N., Sarda-Esteve,
1173 R., Petit, J.-E., and Kukui, A.: Role of Heterogeneous Reactions in the
1174 Atmospheric Oxidizing Capacity in Island Environments, *Environ. Sci. Technol.*,
1175 59, 3153–3164, <https://doi.org/10.1021/acs.est.4c11647>, 2025.
- 1176 Yang, G., Liu, Y., and Li, X.: Spatiotemporal distribution of ground-level ozone in
1177 China at a city level, *Sci Rep*, 10, 7229, [https://doi.org/10.1038/s41598-020-](https://doi.org/10.1038/s41598-020-64111-3)
1178 [64111-3](https://doi.org/10.1038/s41598-020-64111-3), 2020.
- 1179 Ye, C., Lu, K., Ma, X., Qiu, W., Li, S., Yang, X., Xue, C., Zhai, T., Liu, Y., Li, X., Li,
1180 Y., Wang, H., Tan, Z., Chen, X., Dong, H., Zeng, L., Hu, M., and Zhang, Y.:
1181 HONO chemistry at a suburban site during the EXPLORE-YRD campaign in
1182 2018: formation mechanisms and impacts on O₃ production, *Atmospheric*
1183 *Chemistry and Physics*, 23, 15455–15472, [https://doi.org/10.5194/acp-23-15455-](https://doi.org/10.5194/acp-23-15455-2023)
1184 [2023](https://doi.org/10.5194/acp-23-15455-2023), 2023a.
- 1185 Ye, C., Lu, K., Ma, X., Qiu, W., Li, S., Yang, X., Xue, C., Zhai, T., Liu, Y., Li, X., Li,
1186 Y., Wang, H., Tan, Z., Chen, X., Dong, H., Zeng, L., Hu, M., and Zhang, Y.:
1187 HONO chemistry at a suburban site during the EXPLORE-YRD campaign in
1188 2018: formation mechanisms and impacts on O₃ production, *Atmospheric*
1189 *Chemistry and Physics*, 23, 15455–15472, [https://doi.org/10.5194/acp-23-15455-](https://doi.org/10.5194/acp-23-15455-2023)
1190 [2023](https://doi.org/10.5194/acp-23-15455-2023), 2023b.
- 1191 Yu, H., De Smedt, I., Theys, N., Sneep, M., Veefkind, P., and Van Roozendaal, M.:
1192 Harmonized cloud datasets for the Ozone Monitoring Instrument (OMI) and
1193 TROPOspheric Monitoring Instrument (TROPOMI) using the O₂–O₂
1194 477 nm absorption band, *Atmospheric Measurement Techniques*, 18,
1195 4131–4163, <https://doi.org/10.5194/amt-18-4131-2025>, 2025.

- 1196 Yu, Y., Cheng, P., Li, H., Yang, W., Han, B., Song, W., Hu, W., Wang, X., Yuan, B.,
1197 Shao, M., Huang, Z., Li, Z., Zheng, J., Wang, H., and Yu, X.: Budget of nitrous
1198 acid (HONO) at an urban site in the fall season of Guangzhou, China,
1199 *Atmospheric Chemistry and Physics*, 22, 8951–8971,
1200 <https://doi.org/10.5194/acp-22-8951-2022>, 2022.
- 1201 Zeng, Y., Zhang, J., Li, D., Liao, Z., Bian, J., Bai, Z., Shi, H., Xuan, Y., Yao, Z., and
1202 Chen, H.: Vertical distribution of tropospheric ozone and its sources of
1203 precursors over Beijing: Results from ~ 20 years of ozonesonde measurements
1204 based on clustering analysis, *Atmospheric Research*, 284, 106610,
1205 <https://doi.org/10.1016/j.atmosres.2023.106610>, 2023.
- 1206 Zhang, H., Ren, C., Zhou, X., Tang, K., Liu, Y., Liu, T., Wang, J., Chi, X., Li, M., Li,
1207 N., Huang, X., and Ding, A.: Improving HONO Simulations and Evaluating Its
1208 Impacts on Secondary Pollution in the Yangtze River Delta Region, China,
1209 *Journal of Geophysical Research: Atmospheres*, 129, e2024JD041052,
1210 <https://doi.org/10.1029/2024JD041052>, 2024.
- 1211 Zhang, H., Shi, C., Ying, C., Weng, S., Ni, E., Zhao, L., Yang, P., Tang, K., Zhou, X.,
1212 Ren, C., Chi, X., Zhou, D., Li, M., Li, N., Liu, T., and Huang, X.: HONO
1213 formation mechanisms and impacts on ambient oxidants in coastal regions of
1214 Fujian, China, *Atmospheric Chemistry and Physics*, 25, 16797–16816,
1215 <https://doi.org/10.5194/acp-25-16797-2025>, 2025a.
- 1216 Zhang, Q., Liu, P., Wang, Y., George, C., Chen, T., Ma, S., Ren, Y., Mu, Y., Song,
1217 M., Herrmann, H., Mellouki, A., Chen, J., Yue, Y., Zhao, X., Wang, S., and
1218 Zeng, Y.: Unveiling the underestimated direct emissions of nitrous acid (HONO),
1219 *Proc Natl Acad Sci U S A*, 120, e2302048120,
1220 <https://doi.org/10.1073/pnas.2302048120>, 2023a.
- 1221 Zhang, X., Tong, S., Jia, C., Zhang, W., Wang, Z., Tang, G., Hu, B., Liu, Z., Wang,
1222 L., Zhao, P., Pan, Y., and Ge, M.: Elucidating HONO formation mechanism and
1223 its essential contribution to OH during haze events, *npj Clim Atmos Sci*, 6, 55,
1224 <https://doi.org/10.1038/s41612-023-00371-w>, 2023b.
- 1225 Zhang, X., Yan, Y., Zhang, N., Wang, W., Suo, H., Jian, X., Wang, C., Ma, H., Gao,
1226 H., Yang, Z., Huang, T., and Ma, J.: The 21st-century wetting inhibits growing
1227 surface ozone in Northwestern China, *Atmospheric Chemistry and Physics*, 25,
1228 9669–9684, <https://doi.org/10.5194/acp-25-9669-2025>, 2025b.
- 1229 Zhang, Y., Zhang, Y., Liu, Z., Bi, S., and Zheng, Y.: Analysis of Vertical Distribution
1230 Changes and Influencing Factors of Tropospheric Ozone in China from 2005 to
1231 2020 Based on Multi-Source Data, *International Journal of Environmental
1232 Research and Public Health*, 19, 12653, <https://doi.org/10.3390/ijerph191912653>,
1233 2022.

1234 Zhou, M., Li, Y., and Zhang, F.: Spatiotemporal Variation in Ground Level Ozone
1235 and Its Driving Factors: A Comparative Study of Coastal and Inland Cities in
1236 Eastern China, *International Journal of Environmental Research and Public*
1237 *Health*, 19, 9687, <https://doi.org/10.3390/ijerph19159687>, 2022.

1238 Zhu, L., Wang, J., Xu, Y., Ma, N., Song, X., Qin, J., Li, B., Tsui, W. B. C., Lv, L.,
1239 and Zhang, T.: Vertical Characteristics of an Ozone Pollution Episode in Hong
1240 Kong Under the Typhoon Mawar—A Case Study, *Remote Sensing*, 17, 3904,
1241 <https://doi.org/10.3390/rs17233904>, 2025a.

1242 Zhu, X., Wang, H., Han, Y., Zhang, D., Liu, S., Zhang, Z., and Liu, Y.:
1243 Reconstructing the VOC–Ozone Research Framework Through a Systematic
1244 Review of Observation and Modeling, *Sustainability*, 17, 7512,
1245 <https://doi.org/10.3390/su17167512>, 2025b.

1246 Zou, T., Xing, C., Xue, J., Li, Q., Tan, W., Wu, Z., and Liu, C.: Transport
1247 characteristics of urban and rural aerosols based on vertical observations and
1248 deep learning predictions, *Atmospheric Research*, 315, 107876,
1249 <https://doi.org/10.1016/j.atmosres.2024.107876>, 2025.

1250

带格式的: 段落间距段后: 0.5 行